International Journal of Heat and Mass Transfer 207 (2023) 124000

Contents lists available at ScienceDirect

International Journal of Heat and Mass Transfer

journal homepage: www.elsevier.com/locate/hmt

Experimental and computational investigation into hydrodynamic and heat transfer characteristics of subcooled flow boiling on the International Space Station

Issam Mudawar*, Jeongmin Lee

Purdue University Boiling and Two-Phase Flow Laboratory (PU-BTPFL), School of Mechanical Engineering, Purdue University, 585 Purdue Mall, West Lafayette, IN 47907, United States

ARTICLE INFO

Article history:
Received 7 December 2022
Revised 16 January 2023
Accepted 18 February 2023
Available online 3 March 2023

Keywords:
Flow boiling
Microgravity
International Space Station (ISS)
Computational fluid dynamics (CFD)
Interfacial force modeling

ABSTRACT

This study is part of a long-term initiative to investigate flow boiling of n-perfluorohexane (n-PFH) under microgravity on the International Space Station (ISS). Investigated are data received from the ISS during 2022 using the Flow Boiling and Condensation Experiment (FBCE) (actual name of experimental payload). FBCE is designed to accommodate one of two test modules, one for flow boiling and another for condensation. Data for the present study are acquired using FBCE's Flow Boiling Module (FBM), which features a rectangular channel of 5.0-mm height, 2.5-mm width, and 114.6-mm heated length. Examined are results for three different mass velocities of 199.9, 799.9, and 2399.9 kg/m^2.s, and heat fluxes corresponding to approximately 20, 40, and 60% of critical heat flux (CHF). Detailed development of the interfacial behavior is captured by high-speed video through the channel's transparent sidewalls. In the Computational Fluid Dynamics (CFD) model, numerical solver is constructed in ANSYS-Fluent wherein the multiphase model is combined with appropriate models for turbulence, surface tension, and interfacial phase change. Also incorporated are momentum source terms governing bubble shear-lift, bubble drag, and bubble dispersion. Accuracy of the CFD predictions is assessed by comparison against both the heat transfer data and video-captured interfacial behavior. Very good agreement is achieved against measured axial profile of heated wall temperatures and further validated by accurately capturing such interfacial features as bubble formation, detachment, coalescence, and downstream wavy vapor layer development. Additionally, the CFD simulations enable prediction of other transport parameters vitally important to understanding evolution of the boiling flow but not possible from experiment, such as cross-sectional profiles of void fraction, fluid velocity, and mixture temperature.

1. Introduction

1.1. Two-phase fluid physics in space applications

Nowadays, since space enables everything from email and global communications, scientific research, and national security, a new phase of the space race has begun. Space will be the next great common resource, globally shared like the oceans or cyberspace, which will lead both governments and companies to competitively invest in future space missions.

As a result of the increase in scope, size, complexity, and duration of space missions, the electric power required for operation and corresponding heat dissipation proportionally increase. Key to success of these missions is ability to reduce size and weight of all thermal management subsystems while tackling the high levels of heat removal.

An important example of these subsystems is the myriad of electronic and power devices onboard space vehicles and planetary habitats, both Lunar and Martian. With the unrelenting quest for more compact and lightweight packaging, these devices and related sub-systems are expected to generate more heat, requiring more effective thermal management strategies to improve reliability and prevent undesired failure. But, achieving these goals is no longer possible with single-phase thermal management schemes which offer comparatively poor heat transfer coefficients. By utilizing both sensible and latent heat of coolant, two-phase thermal management schemes yield a one to two orders of magnitude higher heat transfer coefficient compared to single-phase counterparts and hence are especially beneficial for systems where high heat fluxes need to be dissipated while maintaining the cooling system small and lightweight.

* Corresponding author.
E-mail address: mudawar@ecn.purdue.edu (I. Mudawar).

https://doi.org/10.1016/j.ijheatmasstransfer.2023.124000
0017-9310/

Nomenclature

A_c	cross-sectional area of channel (mm^2)
Bo	Boiling number
c	cell size (mm)
C_D	bubble drag coefficient
C_L	coefficient in Eq. (18)
d_b	bubble diameter (mm)
E	energy per unit mass (J/kg)
G	mass velocity (kg/m^2s)
g	gravitational acceleration (m/s^2)
g_e	terrestrial gravitational acceleration (m/s^2)
H	longer dimension of channel's cross-section (mm)
h	latent heat (J/kg); heat transfer coefficient (W/m^2K)
h_{fg}	latent heat of vaporization (J/kg)
H_{tc}	distance between thermocouple bead and wetted surface of copper slab (mm)
I	turbulence intensity
K	proportionality constant in Eq. (21)
k_{eff}	effective thermal conductivity (W/m•K)
k_s	thermal conductivity of copper slab (W/m.K)
L_a	adiabatic length of flow channel in experiment (mm)
L_d	development length of flow channel in experiment (mm)
L_e	exit length of flow channel in experiment (mm)
$L_{entrance}$	adiabatic entry length in computational domain (mm)
L_{exit}	adiabatic exit length in computational domain (mm)
L_h	heated length of flow channel (mm)
$\dot{m}$	volumetric mass transfer rate (m^3/s)
P	pressure (Pa)
P_h	heated perimeter of channel (=2 W) (mm)
q''	heat flux (W/m^2)
q''_i	local heat flux passing through copper-fluid interface (W/m^2)
r	mass transfer intensity factor
Re	Reynolds number
S_c	bubble collision dispersion force term (N/m^3)
S_D	drag force term (N/m^3)
S_E	source term in energy equation (W/m^3)
S_M	source term in momentum equation (N/m^3)
S_{sl}	shear-lift force term (N/m^3)
S_{st}	surface force term (N/m^3)
T	temperature (°C, K)
ΔT_w	wall superheat (°C, K)
t	time (s)
u	velocity (m/s)
u'	turbulent fluctuating component of velocity (m/s)
u_c	compressive velocity (m/s)
u_r	velocity difference between liquid and vapor (m/s)
u_t	liquid fluctuation velocity due to bubble agitation (m/s)
W	shorter (heated) dimension of channel's cross-section (mm)
x	coordinate in computational domain (mm)
x_e	thermodynamic equilibrium quality
y	coordinate in computational domain (mm)
y^+	dimensionless distance perpendicular to channel walls
z	axial coordinate in computational domain (mm)

Greek symbols

α	volume of fraction; void fraction
α_{max}	dense packing limit
θ	contact angle (°)
κ	interfacial curvature (m^{-1})
μ	dynamic viscosity (kg/m•s)
ρ	density (kg/m^3)
σ	surface tension (N/m)
ψ	ratio of average heat flux to single phase heat flux based on heated surface area

Subscripts

avg	average
c	condensation
e	evaporation
f	liquid
g	vapor
i	interface
in	inlet
m	mixture
sat	saturation
sp	single-phase liquid
sub	subcooling
tc	thermocouple
w	heated wall

Acronyms

CFD	Computational Fluid Dynamics
CHF	critical heat flux
CLSVOF	Coupled Level-Set Volume-of-Fluid
CSF	Continuous Surface Force
FBCE	Flow Boiling and Condensation Experiment
FBM	Flow Boiling Module
FDB	fully developed boiling
FIR	Fluid Integrated Rack
ISS	International Space Station
LS	Level-Set model
nPFH	n-Perfluorohexane
NVG	net vapor generation
ONB	onset of nucleate boiling
PDB	partially developed boiling
PFM	Phase Field method
SST	Shear-Stress Transport
VOF	Volume-of-Fluid

Improved understanding of two-phase fluid physics is also vitally important to other space applications, including nuclear fission/Rankine power cycle for future space missions to the Moon, Mars, and deep space, vapor compression heat pumps for future Lunar and Martian habitats, advanced life support in spacecraft and space stations, cryogenic fluid management in nuclear thermal propulsion systems, and in-space cryogenic fuel depots.

The buoyancy effect created by density difference between liquid and vapor in the presence of a gravitational field plays a crucial role in defining the vapor motion relative to the liquid. The body force induced by buoyancy encourages bubbles to detach from the wall, aiding in delayed formation of insulating vapor layer (blanket) and ensuing uncontrolled increase in temperature at high heat fluxes. In the absence of body force in microgravity, flow boiling dynamics are dominated by surface tension and flow inertia, which combined control all aspects of flow boiling evolution along a heated channel. In absence of buoyancy effects, there is potentially higher likelihood for vapor bubbles to coalesce into partial or continuous vapor blankets and therefore greater propensity in microgravity for critical heat flux (CHF) to take place. CHF can be described as severe degradation in heat transfer coefficient due to loss of liquid access to the heating surface, and its magnitude is

highly dependent on prevailing gravitational acceleration. In situations involving heat-flux-controlled surfaces, it could trigger an unsteady and uncontrollable escalation in the surface temperature, potentially culminating in device materials melting, burning, or undergoing other forms of permanent damage. It is for these reasons that CHF is recognized as the most important design and safety parameter for most terrestrial and space applications involving heat-flux-controlled surfaces.

Since the mid-1980s, investigators from the Purdue University boiling and Two-Phase Flow Laboratory (PU-BTPFL) have aimed to construct models as well as recommend practical design guidelines for two-phase cooling strategies adopted to a variety of terrestrial applications. Capillary-driven schemes [1] (e.g., conventional heat pipe, capillary pumped loop, loop heat pipe) rely on surface tension for coolant circulation, without the need for a pump. Also lacking a pump is pool boiling thermosyphon [2], which features rather simple and inexpensive construction. Another so called *semi-passive* cooling scheme is one utilizing falling films [3], which requires only a small pump to maintain the coolant circulation, aided largely by buoyancy. Higher heat flux applications are better managed using pump-driven channel flow boiling [4], where flow inertia is vital to flushing vapor away from, and maintaining liquid access to, the heated surface. When it comes to very high flux situations, three different pump-driven schemes compete for most superior cooling performance: mini/micro-channel flow boiling [5], jet impingement [6], and spray [7]; each provides unique operational advantages but also potential shortcomings. Even more effective are *hybrid* schemes [8] combining merits of two or more of the above schemes.

Aside from the need to reduce weight and volume and tackle high heat fluxes, choice of cooling scheme for space applications is highly dependent on type of cooling hardware adapted. Most common among spacecraft avionics are *cold plates*, plate-shaped aluminum modules featuring a single coolant inlet and single outlet and within which the coolant is circulated in rectangular flow passages with the electronics or power devices mounted upon one of its outer surfaces. A complete thermal management might include multiple cold plates connected to a main cooling loop in a variety of series/parallel arrangements. It is for these reasons that channel flow boiling is deemed best contender for thermal management of avionics in space applications and is therefore the primary focus for the present study.

1.2. Prior observations on flow boiling in microgravity

As mentioned earlier, since many of the thermal subsystems in space applications involve single-phase fluid and heat transfer processes, an urgent shift toward two-phase fluid operation is required for improved energy-to-mass ratios, especially in space missions that are expected to tackle massive quantities waste heat. The problem is that, because most data available for the behavior of two-phase flows have been obtained in Earth's gravity, most insights presented in textbooks and published articles are for one-g_e operation. However, the influence of gravity is profound and would give a completely invalid blueprint for predicting microgravity two-phase flows, especially for large scale systems. As shown in Fig. 1, operating space applications span a fairly broad range of gravities. Except for fighter aircraft, satellite, Earth-orbiting vehicles, and space stations work under environment of between Martian and micro gravities. This creates an urgent need to investigate two-phase flows in gravity levels between 0.38 g_e and μg_e.

Several types of platforms have been built to attain actual microgravity conditions, the most well-known and useful of which for investigation of two-phase flows is to use parabolic flight. Saito et al. [9] performed water flow boiling experiments in a 25-mm × 25-mm square channel involving an 8-mm diameter and 200-mm length rod electrical heater mounted along the channel's central axis to examine the effects of reduced gravity on the flow boiling regime and heat transfer characteristics. Bubble formation and flow structure in both Earth and reduced gravities between −0.01 and 0.01 g_e were compared. They observed bubbles to slide along the heated rod and coalesce into large bubbles in reduced gravity while frequent detachment into the bulk flow took place in 1 g_e, resulting in a stratified flow. Interestingly, gravity barely impacted the local heat transfer coefficient along the rod's surface. Ma and Chung [10] conducted forced-convection boiling of FC-72 in a drop tower, which is an alternative to parabolic flight also producing microgravity conditions, with an effective acceleration on the order of 10^{-4} g_e. The differences in the bubble behavior became distinct at higher surface temperatures and lower flow rates. The bubbles in reduced gravity coalesced into bigger bubbles at high temperatures. However, they suggested that the effects of gravity on bubble behavior would diminish at high flow rates. In terms of the heat transfer characteristics, they also hypothesized that gravity level would be irrelevant where flow inertia achieves dominance over body force above a certain value of flow rate.

Because of high cost, hardware complexity, and sparse data that researchers are able to obtain from short-duration microgravity experiments on Earth, the period of taking two-phase transport data in reduced gravity is quite short. Zhao [11] performed short-term microgravity experiments utilizing a drop tower, which provided only 3.6 s for acquiring data. Longer periods are possible with parabolic flight experiments. A single flight campaign often includes 30 to 40 parabolic flight maneuvers, each yielding a 15- to 25-s microgravity period after a short duration of high levels of gravity [9,12]. Galbiati and Andreini [13] investigated two-phase capillary flow along a small diameter tube under terrestrial conditions to simulate a microgravity-equivalent system.

Even though prior investigators have successfully simulated microgravity environments in Earth gravity for investigation of two-phase flow and heat transfer, they often experienced great difficulty acquiring steady-state data within the experiment's short duration or failed to cover a wide range of operating conditions.

1.3. Computational fluid dynamics (CFD) modeling of two-phase flow in reduced gravity

To overcome the limitations of conducting experiments in simulated microgravity environments, recent research has shown especial interest in relying on Computational Fluid Dynamics (CFD) to predict reduced gravity two-phase fluid physics. Table 1 [14–23] presents a summary of computational works on two-phase flow in reduced gravity. They relied on a variety of interface tracking models to obtain a sharp interface, compute accurate mass transfer by phase change, and consequently evaluate two-phase heat transfer. Most popular among the models used are *Volume-of-Fluid* (VOF) [14,20,23], *Level-Set* (LS) [15,16], *Coupled Level-Set Volume-of-Fluid* (CLSVOF) [17,19,22], and *Phase Field method* (PFM) [18].

The VOF method is the most widely used interface-capturing approach, solving a continuity equation for volume fraction of each phase to obtain the values of void fraction in fluid cells. It is comparatively efficient and provides accurate interfacial mass conservation calculations, albeit with a comprised ability to capture sharp interfaces. The LS method is another popular interface tracking method, defining a level-set function as a signed distance from the interface. It is more effective than VOF in ability to capture sharp interfaces but comprises accuracy of interfacial mass conservation. The CLSVOF is a combination of the VOF and LS methods, taking advantage of VOF's superior interfacial mass conservation and LS's ability to capture sharp interfacial features [17]. The PFM method is based on the fluid free energy model, adopting the Cahn-Hilliard

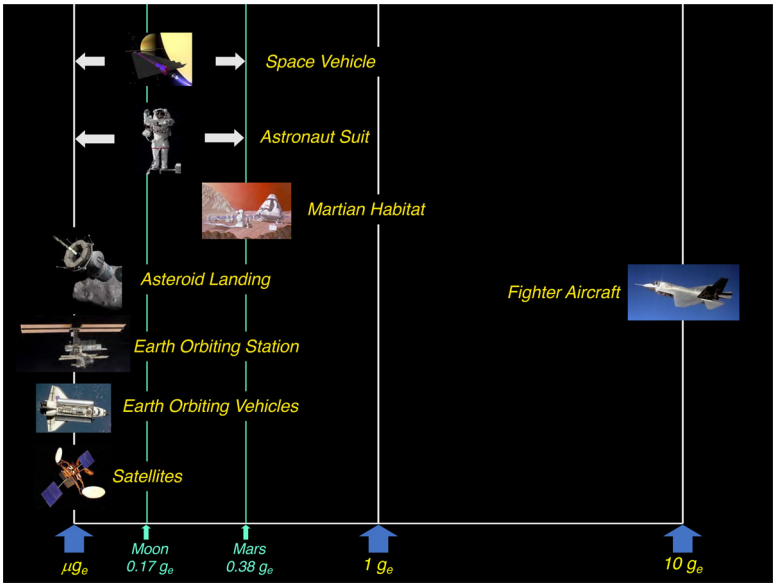

Fig. 1. Range of gravities important to study of two-phase flow and heat transfer in space and aircraft applications.

Table 1
Summary of prior CFD studies for reduced gravity two-phase flow.

Author(s)	Gravity Levels (g/g_e)	Working Fluid(s)	Remarks
Georgoulas et al. [14]	$0.059 \leq g/g_e \leq 1.1203$	R113, R22, R134a	VOFSP3D
Dhruv et al. [15]	$10^{-4} \leq g/g_e \leq 1$	FC-72	LSS, MP3D
Banerjee et al. [16]	$g/g_e = 0.014, 1$	Water, FC72	LSSP2D
Chakraborty et al. [17]	$10^{-2} \leq g/g_e \leq 1$	Air-Water	CLSVOFSA2D
Yi et al. [18]	$0.04 \leq g/g_e \leq 0.12$	Water	PFMSP2D
Guo et al. [19]	$0.11 \leq g/g_e \leq 1$	MNF (Magnetic nano fluid)	CLSVOFMP2D
Li, Fang [20]	$1 \leq g/g_e \leq 9$ g	Water-Al_2O_3	VOFMF2D
Wang et al. [21]	$0.01 \leq g/g_e \leq 1$	LH_2	VOFMP2D
Zheng et al. [22]	$10^{-4} \leq g/g_e \leq 1$	LH_2	CLSVOFMF3D
Bahreini et al. [23]	$g/g_e = 0.05, 1$	HFE-7100	VOFMF2D

CLSVOF: Coupled level-set and volume-of-fluid; PFM: Phase field method.
M: Multiple channels; S: Single channel.
A: Adiabatic; F: Flow boiling; P: Pool boiling.

equation [25] to distinguish the free interface and phases with phase field variables [18]. All the CFD methods described above have their own strengths when it comes to capturing a less diffused interface, maintaining mass conservation at the interface, or computing local void fraction.

However, most of them focus on very small and confined domains, such as single bubble growth, which would be helpful to validate the CFD approach. But, from a practical point of view, they lack suitability to modeling practical large-domain two-phase cooling systems, in terms of inability to address interactions between multiple bubbles, bulk fluid motion, and two-phase heat transfer, let alone that some are unusually computationally intensive and therefore both costly and very time consuming. A few studies successfully simulated multiple bubble behavior, but they were limited to pool boiling only. Overall, majority of researchers have relied on VOF for tracking interfaces in flow boiling because of this model's both computational efficiency when tackling large flow boiling domains and superior interfacial mass conservation capability. It is for these reasons that VOF is used in the present study to capture fluid flow and heat transfer characteristics for flow boiling in a rectangular channel.

VOF is an interface-tracking technique and involves solving a continuity equation for volume fraction of each phase, along with a single momentum equation and single energy equation, both shared by the two phases, in which each physical property is expressed as a function of properties of the individual phases weighted with respect to volume fraction. By not accounting for momentum of individual phases using separate momentum equations, VOF suffers limitations in ability to predict interfacial behavior in flow situations involving a discrete fluid in another continuous fluid (e.g., bubbly, slug, and mist/droplet flows). It numerically solves the Navier-Stokes equation and implicitly accounts for interfacial forces between the phases. Given that discontinuity of interfacial pressure at interfacial cells is not precisely considered, the pressure force is weight-averaged in terms of ratio of distance between cell centers to distance between cell center and interface, leading this numerical treatment to become less accurate where severe interface distortions are present, such as bubble distortion during flow boiling [26]. Other drawbacks—brought about mostly by use of a single momentum conservation equation, are compromised ability to account for local velocity differences between the phases, or interfacial force and momentum interactions, such as shear-lift, drag, wall lubrication, virtual mass, and turbulent dispersion. Additionally, the inability to accurately account for interfacial force and momentum interactions leads to errors in predicting other vital aspects of flow boiling in microgravity, especially bubble departure, since body force is reduced to zero and shear-lift force is now the most dominant, which renders predictions of flow regime development along the flow channel quite elusive.

Clearly, when it comes to modeling dispersed liquid-vapor flows, predictive potential using VOF is highly dependent on the accuracies of individual closure relations for interfacial forces. Un-

fortunately, because of both the difficulty in estimating key interfacial parameters and numerical instability (convergence issue), the effects of additional important interfacial forces on two-phase flow and heat transfer have received little attention in published literature. It is therefore a primary goal of the present study to provide new guidance regarding the incorporation of important interfacial forces to enhance the predictive potential of the CFD model.

1.4. Objectives of present study

The present study is a part of a joint endeavor between PU-BTPFL and the NASA Glenn Research Center that was initiated in 2012 to develop the *Flow Boiling and Condensation Experiment* (FBCE) (actual name of the experimental facility), which was deployed on the *International Space Station* (ISS) in 2021 and began transmitting microgravity data for the flow boiling portion in early 2022. Overall, FBCE represents NASA's largest, most complex, and most capable phase change facility (in terms of channel size, power input, and flow rate) developed to date. This endeavor involves a multitude of experimental, theoretical, and computational tasks, all aimed at better understanding the effects of reduced gravity on flow boiling and flow condensation. Focused entirely on the flow boiling portion, the present study provides CFD simulations of flow boiling of n-Perfluorohexane (nPFH, C_6F_{14}) along a rectangular channel that is heated along two opposite walls. Predicted results are validated against both heat transfer measurements and high-speed video records of interfacial behavior along the channel.

The computational results presented will be for select operating conditions from the experiments, including different mass velocities and heat fluxes with subcooled inlet conditions, with the aim of predicting both fluid flow and heat transfer characteristics under microgravity. The VOF method is adopted to track details of the interfacial behavior, including bubble nucleation, growth, and departure from the heated wall, as well as both coalescence and break-up. A 3D computational domain is used, which captures the precise size and shape of the heated portion of the experimental channel with identical inlet and wall heating conditions, also accounting for conjugated heat transfer. A key feature of the CFD scheme is the modeling of (i) shear-lift force, (ii) bubble collision dispersion force, and (iii) drag force, which are implemented as *user-defined functions* (UDFs) to compensate for fundamental weaknesses of previous VOF-based models. It will also be shown how the CFD simulations facilitate predictions of vital characteristics of flow boiling which cannot be easily obtained from experiment, including spatial variations of fluid velocity, fluid temperature, and void fraction, both across and along the channel.

2. Experimental methods

2.1. Construction of the flow loop and flow boiling module (FBM)

As indicated above, the test facility employed in this study is NASA's Flow Boiling Condensation Experiment (FBCE), which commenced operation on the ISS in February 2022. The experimental results used for the assessment of the CFD simulations were acquired from the ISS tests. The key component of the facility from which the data is obtained is the Flow Boiling Module (FBM) shown in Fig. 2(a), wherein fluid flow and heat transfer characteristics are measured, with interfacial behavior captured using high-speed video at a frequency of 2000 frames per second. As shown in Fig. 2(b), FBCE is comprised of several subassemblies, which were launched to the ISS in August 2021 aboard the Cygnus spacecraft via Northrop Grumman's Antares Rocket. The FBCE subassemblies were subsequently integrated together in the ISS inside the Fluid Integrated Rack (FIR).

Fig. 2(c) shows a schematic diagram of the two-phase flow loop, which is configured to supply n-Perfluorohexane to the FBM at the desired flow rate, pressure, inlet subcooling, and flow rate. The working fluid is degassed prior to commencing any series of tests. During the flow boiling experiments, the fluid is circulated within the loop with the aid of a magnetically coupled gear pump. The fluid then passes through a filter, followed by a Coriolis flowmeter, before entering a preheater, which is used to set liquid subcooling at the inlet to the FBM. Phase change occurs within the flow channel of the FBM, and the exiting two-phase mixture passes through a heat exchanger to return the mixture to a single-phase liquid state. The liquid then enters a junction attached to a gas-pressurized accumulator, which serves the purpose of setting a precise reference pressure point for the entire flow loop and compensates for volume changes associated with vapor generation. Exiting the accumulator junction, the fluid, now in liquid state, is returned to the pump, completing a full flow cycle.

Fig. 3(a) shows the construction of FBM: three plates of transparent polycarbonate plastic (Lexan) compressed between two aluminum support plates, and two oxygen-free copper slabs inserted into slots milled into the top and bottom Lexan plates. O-ring seals are fitted into grooves in the Lexan plates to guard against leaks. A honeycomb flow straightener is affixed upstream to help straighten the incoming flow and eliminate any eddies. The fluid is heated along the heated length of $L_h = 114.6$ mm by a series of resistive heaters soldered to the back of each copper slab. The channel, which is milled into the middle polycarbonate plate, features a rectangular cross-section of dimensions $W = 2.5$ mm and $H = 5$ mm, with heating possible along either one or both short walls W. An entry development length of $L_d = 327.9$ mm is used to ensure fully developed flow upstream of the heated length, and a downstream 60.7 mm long adiabatic length comes after the heated length. Fig. 3(b) presents the construction of the copper slabs with details on how six resistive heaters are affixed to the slab's back. To achieve axially uniform heating, the 188−Ω resistive heaters for each copper slab are connected electrically in parallel and powered by a variable voltage transformer. Fig. 3(c) shows layout of two sets of seven type-E thermocouples inserted into shallow holes along the centerline of each copper slab just upstream and downstream of each resistor. The thermocouples provide axial profiles of heated wall temperature which are essential to assessing the predictive accuracy of the CFD simulations. Notice that the longer sidewalls (H), being made from insulating Lexan, are adiabatic, and their transparency is essential for high-speed video imaging of interfacial features along the flow channel's heated length. The reader is advised to refer to the authors' prior study [27] for additional details concerning the experimental setup, operating procedure, flow visualization technique, instrumentation, and measurement uncertainty.

It is important to note that all present tests were performed under microgravity with the flow channel in the ISS. Additionally, all tests discussed in the present study were performed with heating applied along both opposite short walls (W), with the goal of promoting flow and heat transfer symmetries across the flow area.

2.2. Data processing

Steady-state datapoints are obtained by averaging the steady portions of the temporal data recorded by the data acquisition system, and further post-processing is performed, with all the fluid properties obtained from NIST-REFPROP [28].

At the FBM inlet, the fluid is in a subcooled liquid state, and the corresponding fluid enthalpy is directly determined from the FBM inlet fluid temperature, T_{in}, and pressure, p_{in}, as

$$h_{in} = h|_{T_{in}, p_{in}}. \quad (1)$$

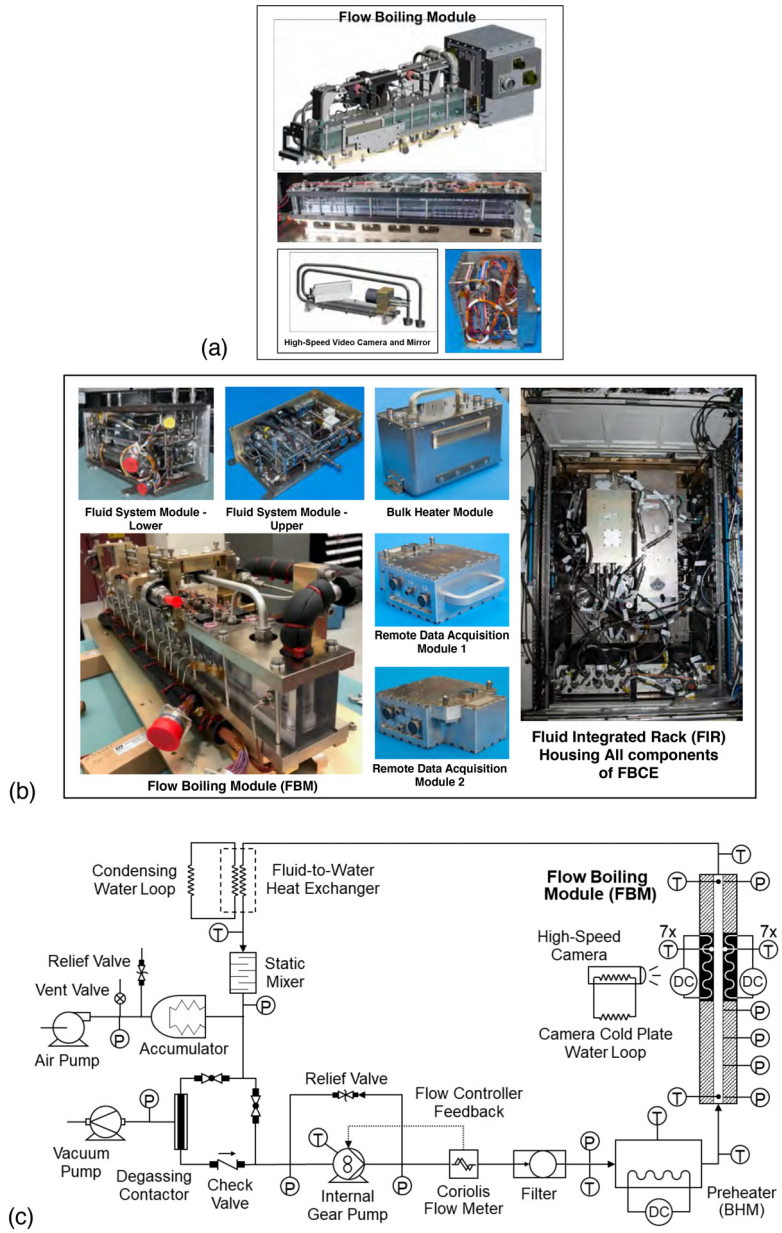

Fig. 2. (a) Image and CAD renderings of the Flow Boiling Module (FBM). (b) Images of FBCE's subassemblies and Fluid Integrated Rack (FIR), and (c) Schematic diagram of experimental two-phase flow loop.

At the FBM outlet, the fluid can contain some vapor, and the fluid enthalpy is calculated from an energy balance over the FBM as

$$h_{out} = h_{in} + \frac{q'' P_h L_h}{\dot{m}}, \tag{2}$$

where q'' is wall heat flux from wetted surface of the copper slabs, $\dot{m}$ mass flow rate, and P_h heated perimeter (2 W).

Thermodynamic equilibrium qualities at both the FBM inlet and outlet are determined as

$$x_e = \frac{h - h_f\big|_p}{h_{fg}\big|_p}, \tag{3}$$

where $h = h_{in}$ or h_{out} is the actual fluid enthalpy at the FBM inlet/outlet, and both h_f, the saturated liquid enthalpy, and h_{fg}, the latent heat of vaporization, are evaluated at the measured inlet/outlet pressure.

As indicated in Fig. 3(c), local wall temperatures are designated as $T_{wi,z}$, where w_i is the heated wall (w_1 or w_2) and z the streamwise measurement location (1 upstream through 7 downstream). Each local wall temperature, T_w, is calculated from the corresponding measured thermocouple temperature, T_{tc}, by assuming a uniform heat flux and one-dimensional heat conduction through distance H_{tc} (= 0.48 mm) within pure copper of thermal conductivity, k_s, as

$$T_w = T_{tc} - \frac{q'' H_{tc}}{k_s}. \tag{4}$$

Both saturation temperature, $T_{sat,z}$, and thermodynamic equilibrium quality, $x_{e,z}$, at these locations are determined by linear interpolation between values at the inlet and outlet. Heated single-phase length is estimated as

$$L_{h,sp} = \frac{GA_c}{q'' P_h}\left(h_{f,Pin} - h_{in}\right), \tag{5}$$

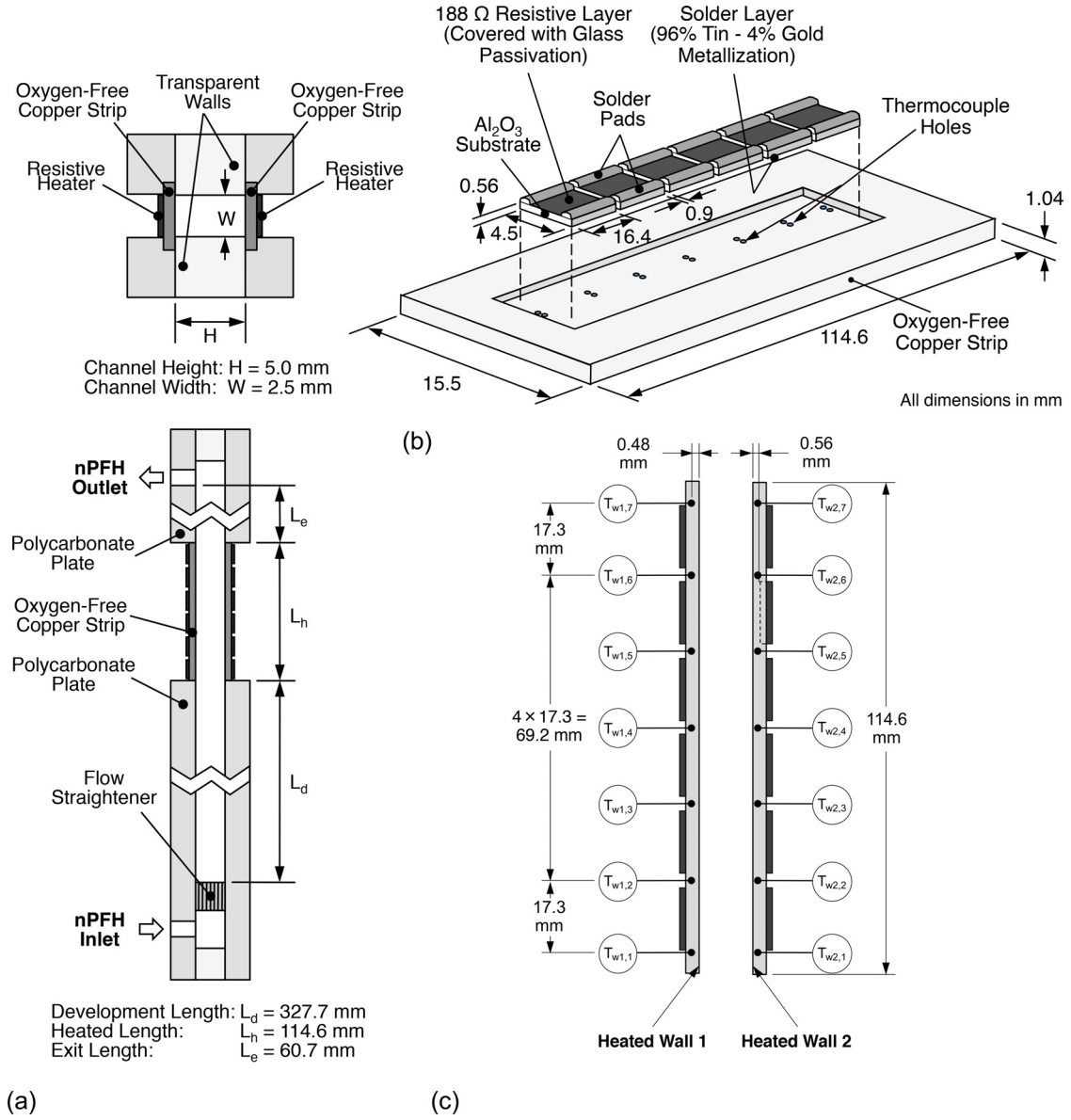

Fig. 3. Schematic representations of (a) overall construction of Flow Boiling Module (FBM), (b) construction of heating strips, and (c) designation of heated walls and local wall temperatures.

where A_c is the channel's cross-sectional area, and saturation temperature at the end of $L_{h,sp}$ (*i.e.*, at location where $x_e = 0$) is estimated by linear interpolation as

$$T_{sat,x=0} = T_{sat}|_{p_{in}} + \left(T_{sat}|_{p_{out}} - T_{sat}|_{p_{in}}\right)\frac{L_{h,sp}}{L_h}. \tag{6}$$

The fluid temperature at the streamwise locations is estimated based on the local fluid state as

$$T_{f,z} = \begin{cases} T_{in} + (T_{sat,x=0} - T_{in})\frac{z}{L_{h,sp}}, & x_{e,z} < 0 \\ T_{sat,z}, & 0 \le x_{e,z} \le 1 \end{cases}. \tag{7}$$

Maximum uncertainties for measurements of absolute pressure, temperature (using thermocouples), temperature (using RTDs), and flow rate are ±0.7 kPa, ±0.5 °C, ±0.5 °C, and ±0.6%, respectively. The maximum measurement uncertainty of FBM heater power input is ±0.3%. The maximum deviation of predictions from experiment for both q'' and q_l'' is 2.21%.

3. Computational methods

3.1. Computational sub-models and key constituent formulations

Subcooled flow boiling in a rectangular channel heated along two opposite walls is simulated under zero gravity with transient analysis in ANSYS-Fluent to track dynamic two-phase fluid flow and heat transfer behavior both across and along the heated length of the flow channel. Aside from the transient analysis, interface tracking, associated with interfacial mass transfer by phase change and surface tension resulting from interfacial curvature, is crucial to accurately determine the detailed interfacial structure. The *Lee mass transfer model* [29] and *Continuous Surface Force* (CSF) *model* [30] are incorporated with the transient VOF method to account for these interfacial effects. The *Geo-Reconstruction scheme*, also known as the piecewise-linear method, and *anti-diffusion treatment* [31] are used, respectively, to help achieve sharp interface

morphology and prevent false interfacial distortion induced by numerical diffusion. The *Shear-Stress Transport* (SST) *k-ω* turbulence model, which also accounts for viscous heating, is used to address turbulence and eddy dissipation effects.

In the present simulations, additional important force terms are accounted for: (i) *shear-lift*, (ii) *bubble collision dispersion*, and (iii) *drag*, to compensate for fundamental shortcomings of VOF. As discussed earlier, despite VOF's popularity for two-phase simulations, given the inherent limitation of using a single momentum equation for both liquid and vapor phases, interfacial forces governed by relative motions between phases are not accurately accounted for. Although the momentum equation incorporated with the VOF model implicitly calculates interfacial forces from computed velocity and pressure fields, the accuracy of these parameters near an interface can be adversely affected in cases where large velocity differences exist between phases [32]. Examples include bubbles which are (1) nucleating but attached to the wall, (2) just detaching from the wall, or (3) migrating across the channel (not in parallel to the dominant flow direction). As shown in the ref. [33], streamlines or vector fields around a bubble attached to the wall penetrate across the bubble interface, failing to capture actual pressure increase near the stagnation point. This issue can erroneously lead to formation of insulating vapor films at the wall and therefore premature CHF.

However, the predictive accuracy of the CFD methodology might be improved further by incorporating additional terms in the momentum equation not precisely computed in the shared fields of velocity and pressure. For flow boiling, shear-lift force and bubble collision dispersion force can encourage the bubbles to detach from the heated wall and prevent excessive coalescence, respectively. Drag force can flush out the bubbles running behind compared to bulk fluid motion. To carefully consider all these forces is important not only to obtain the local flow boiling configuration but also to evaluate heat transfer. Details will be discussed in a later section.

To expedite computations, the following assumptions are in the present simulations:

(1) Liquid and vapor phases are both incompressible and immiscible.
(2) Thermophysical properties of liquid and vapor are constant as pressure drop across the channel for all cases considered is miniscule.
(3) The heated wall is smooth. and details of wall cavity sizes and distributions are not incorporated into the model.
(4) Heat loss by conduction through the test module and external natural convection are ignored given the excellent insulating design of FBM.

3.1.1. Volume-of-fluid (VOF) model

Volume fractions for vapor are computed for the entire computational domain except the solid wall by solving the following continuity equation using the VOF formulation:

$$\frac{\partial \alpha_g}{\partial t} + \nabla \cdot (\alpha_g \vec{u}_g) = \frac{1}{\rho_g} \sum \left(\dot{m}_{fg} - \dot{m}_{gf} \right), \tag{8}$$

where α, t, u, ρ, $\dot{m}_{fg}$ and $\dot{m}_{gf}$ are volume fraction, time, velocity, density, and mass transfer rate by evaporation and condensation, respectively. The volume fraction for liquid is not solved but computed based on the constraint that the sum of volume fractions in each cell is equal to unity,

$$\alpha_f = 1 - \alpha_g. \tag{9}$$

The physical properties appearing in the governing equations are expressed as functions of properties of individual phases weighted with respect to the volume fraction.

The *Geo-Reconstruction* method is incorporated with the VOF model to predict interface shapes. Excess numerical diffusion in interfacial cells, which can arise from fluid advection in high aspect-ratio cell, is suppressed by *anti-diffusion treatment*, adding a negative diffusion source term, $-\nabla \cdot (\vec{u}_c \alpha(1-\alpha))$, in the volume fraction equation, where $\vec{u}_c$ is compressive velocity that prevents dispersion in the direction normal to the interface.

A single momentum conservation equation and single energy conservation equation are solved for the entire computational domain. They are expressed, respectively, as

$$\frac{\partial}{\partial t}(\rho \vec{u}) + \nabla \cdot (\rho \vec{u}\vec{u}) = -\nabla P + \nabla \cdot \left[\mu \left(\nabla \vec{u} + \nabla \vec{u}^T \right) \right] + \rho \vec{g} + \vec{S}_M \tag{10}$$

and

$$\frac{\partial}{\partial t}(\rho E) + \nabla \cdot (\vec{u}(\rho E + P)) = \nabla \cdot \left(k_{eff} \nabla T \right) + S_E, \tag{11}$$

where P, μ, g, S_M, E, k_{eff}, T, and S_E and refer, respectively, to pressure, dynamic viscosity, gravitational acceleration, momentum source term, internal energy, temperature, effective conductivity, and heat source term, the latter being the mass transfer rate multiplied by the latent heat of vaporization. As discussed earlier, additional momentum source terms adopted in the present study account for important forces not accounted for in the conventional VOF model.

3.1.2. Phase change model

Different models have been adopted in prior studies to calculate mass transfer rate across interfaces. For example, Schrage [34] and Tanasawa's [35] models allow for pressure and temperature jumps, respectively, across the interface when calculating mass transfer rate by evaporation and condensation. Another method to account for interfacial phase change is the Rankine-Hugoniot jump condition [36], which is based on net energy transfer by conduction across the interface.

Magnini and Thome [37] utilized the Schrage model to simulate slug flow within a microchannel. Chen et al. [38] used net interface heat flux around small bubble nuclei, relying on an empirical model for nucleation site density.

While the Schrage and Tanasawa models are based on sound physical premises, they require pre-existing interfaces to calculate interfacial mass transfer rate when marching forward along the computational domain. Their dependence on the gradient of void fraction, $|\nabla \alpha_g|$, which has non-zero value only at interfaces, therefore greatly complicates modeling of flow boiling with a subcooled liquid inlet (also flow condensation with a superheated vapor inlet), which lack pre-existing interfaces. It is noted that all the cases simulated in the present study involve subcooled inlet conditions.

Aside from these models, the Lee model [29] has shown remarkable versatility in tackling different phase change configurations and broad ranges of operating conditions using a rather simple formulation for mass transfer rate by evaporation and condensation,

$$\dot{m}_{fg} = r_e \alpha_f \rho_f \frac{\left(T_f - T_{sat} \right)}{T_{sat}} \quad \textbf{for evaporation} \tag{12}$$

and

$$\dot{m}_{gf} = r_c \alpha_g \rho_g \frac{(T_{sat} - T_g)}{T_{sat}} \quad \textbf{for condensation}. \tag{13}$$

where r_e and r_c are *mass transfer intensity factors* for evaporation and condensation, respectively, which will be discussed below. One important attribute of the Lee model is reliance on volume fractions of liquid and vapor, rather than vapor volume fraction gradient across the interface, to determine the mass transfer rate.

Therefore, unlike the prior models, the Lee model does not require pre-existing interfaces when tackling flow boiling with subcooled liquid conditions at the inlet. But, like the Schrage and Tanasawa models, a major challenge in calculating interfacial mass transfer rate is dependence on the mass transfer intensity factors, whose magnitudes are neither theoretically determined nor are they universal. Therefore, the magnitudes of r_e and r_c must be carefully tuned based on flow configuration and geometry, working fluid, and operating conditions, guided by the requirement to ensure small temperature difference between the interface and saturated vapor, and need to prevent numerical divergence. In effect, optimum values for r_e and r_c are determined by realizing best agreement with both (i) measured wall temperatures, and (ii) video-captured interfacial behavior along the channel. The impact of the magnitude of mass transfer intensity factors was discussed in great detail in the authors' recent works [33,39] for the same flow channel examined in the present study. The mass intensity factors for this study were carefully investigated and selected as $r_e = 100$ and $r_c = 20$.

3.1.3. Additional momentum equation terms

3.1.3.1. Surface tension terms. Surface tension effects at interfaces are modeled by incorporating an addition force term S_{st} which is calculated using the *Continuum Surface Force (CSF) Model* [30],

$$S_{st} = \frac{2\rho_m}{\rho_f + \rho_g}\sigma\kappa\nabla\alpha, \tag{14}$$

where ρ_m and σ are the volume-averaged density of the mixture and the surface tension, respectively, and κ is the interface curvature defined in terms of divergence of the unit surface normal,

$$\kappa = \nabla\cdot\hat{n} = \nabla\cdot\left(\frac{\nabla\alpha}{|\nabla\alpha|}\right). \tag{15}$$

For the wall adhesion, the liquid-vapor interface normal for a cell near the wall is given by

$$\hat{n} = \hat{n}_w\cos\theta_w + \hat{t}_w\sin\theta_w, \tag{16}$$

where $\hat{n}_w$and $\hat{t}_w$ are the wall's unit normal and tangential vectors, respectively, and θ_w is the contact angle at the wall, which is determined by the wall superheat, ΔT_w, according to [40]

$$\theta_w = 17.4(\Delta T_w)^{0.323}. \tag{17}$$

3.1.3.2. Shear-lift force. Shear-lift force induced by the shear rate of oncoming flow should be carefully examined as it is poorly predicted by the conventional VOF method and found to affect bubble detachment form the wall significantly. In addition, for a typical bubble of around 0.3 mm, shear-lift force is of the same order of magnitude as surface tension and unsteady drag forces and therefore has a significant impact on near-wall bubble dynamics.

To improve the prediction of near-wall bubble behavior and thus heat transfer, the shear-lift force formulation by Mei and Klausner [41] is employed as a source term in the momentum equation using a user-defined function (UDF) in ANSYS-Fluent. A correlation was developed using data for a wide range of Reynolds numbers and is given as

$$S_{sl} = \frac{1}{8}\pi C_L\rho_f u_r^2 d_b^2, \tag{18}$$

where

$$C_L = 3.877G_s^{1/2}\times\left[\mathrm{Re}_b^{-m/2} + \left(0.344G_s^{1/2}\right)^m\right]^{1/m}, \textbf{ with } \mathbf{m = 4} \tag{19}$$

and

$$G_s = \frac{1}{2}\left|\frac{du_r}{dy}\right|\frac{d_b}{u_r}, \tag{20}$$

In the equations above, G_s is the dimensionless shear rate based on relative velocity u_r $(= u_f - u_g)$ between the vapor bubble and liquid, d_b is the bubble diameter, and Re_b is the bubble Reynolds number based on bubble diameter as characteristic length.

3.1.3.3. Bubble collision dispersion force. Predictive accuracy of the CFD method might be improved further by incorporating effects of another force not accounted for in the conventional VOF formulation. Origins of this force can be described as follows. Detached bubbles from the heated wall experience turbulence-driven random collisions with neighboring bubbles. Absent this effect in the VOF model, bubbles would coalesce more often along the flow channel, culminating in exaggerated formation of non-physical large bubbles, especially for lower mass velocities. Sharma et al. [42] modeled the *turbulence-induced bubble collision force* responsible for bubble diffusion without significant coalescence. This force was shown to describe the lateral movement of bubbles in flow boiling and resulted in a flatter void fraction profile in the channel's cross-section. Note that bubbles can be classified into two major groups [43]: (i) spherical and distorted bubbles, and (ii) slug and churn-turbulent bubbles. The original formulation of the bubble collision dispersion force model is best suited for bubbly flow, which is dominant in the present study. According to [42], the bubble collision dispersion force per unit volume of mixture can be modeled and computed according to

$$S_c = -\left(K\frac{\rho_f u_t^2}{2\alpha_{\max}^{2/3}}\right)f(\alpha)\nabla\alpha, \tag{21}$$

where $\alpha_{\max}$ and K are the *dense packing limit* and a proportionality constant, with recommended values for bubbly flow of 0.62 and 1. Also in Eq. (21), u_t is liquid fluctuating velocity due to liquid agitation, which represents effects of turbulence intensity on bubble dispersion, and $f(\alpha)$ is defined as

$$f(\alpha) = \alpha^{2/3}\left[1 - \left(\frac{\alpha}{\alpha_{\max}}\right)^{1/3}\right]^{-1}. \tag{22}$$

To investigate possible improvements to the CFD predictions, the bubble collision dispersion force formulation, which addresses the probability of collision, is employed as a source term in the momentum equation using a user-defined function (UDF). It is incorporated in the other UDF describing shear-lift force as described earlier. Based on Eq. (21), the bubble collision dispersion force formulation requires determining the liquid fluctuating velocity, u_t. It is both computationally complex and expensive to determine u_t around every bubble along the heated portion of the channel since bubble size, shape, and motion, and therefore bubble-induced liquid turbulence all vary with space and time. In the present subcooled flow boiling configuration with one-sided wall heating, detached vapor bubbles change their shape and size due to both bubble-induced turbulence and condensation, which affects both interfacial forces and bubble virtual mass. As each bubble deforms in an anisotropic fashion during the flow boiling process, it is extremely difficult to determine the exact magnitude of the local fluctuating velocity along the bubble interface. Because of these complicating factors, the present study uses a net velocity difference between vapor phase velocity at each cell and average velocity of liquid flow, which is updated every iteration.

3.1.3.4. Drag force. In addition to the forces discussed above, another force term is incorporated in the momentum equation to account for drag effects. A drag force is applied to vapor bubbles whose velocity is lower than liquid velocity, and it is given by

$$S_D = \frac{3}{4}C_D\frac{\rho_f\alpha u_r|u_r|}{d_b}, \tag{23}$$

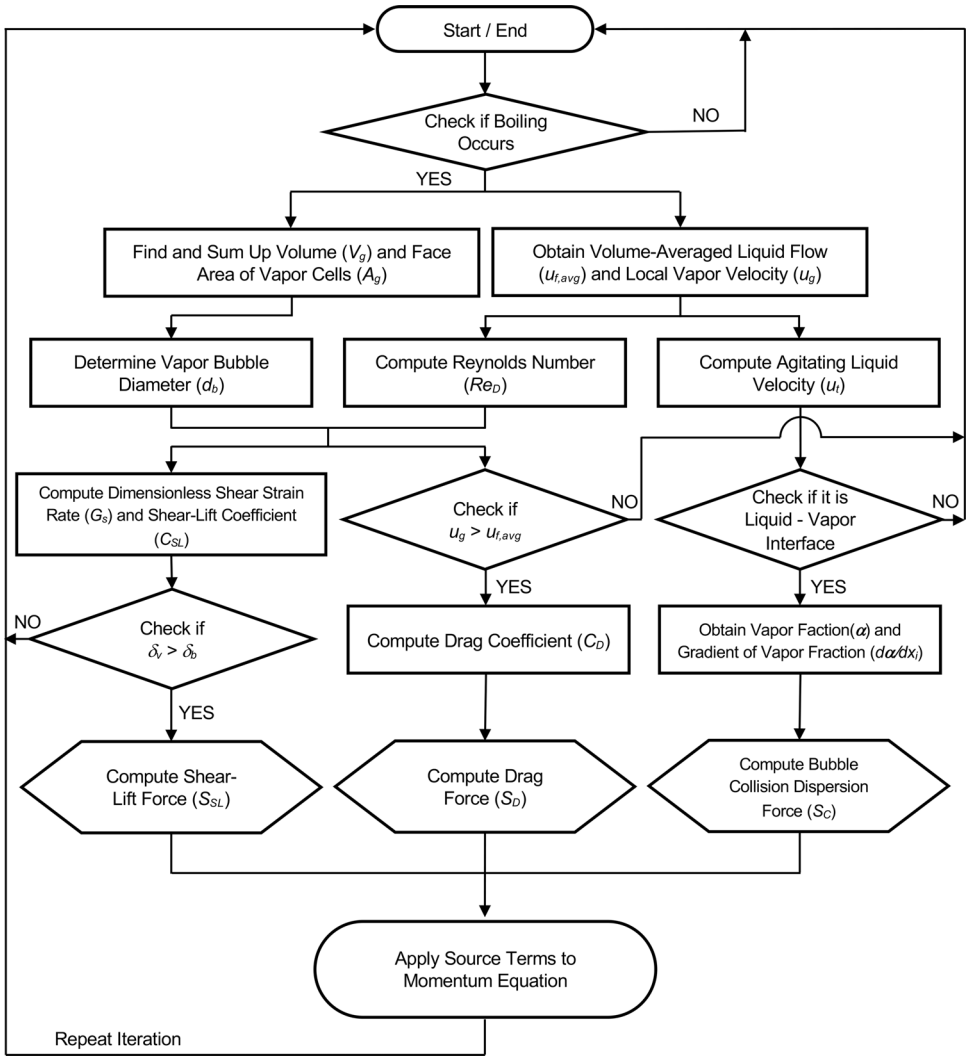

Fig. 4. Flowchart for the model computations, including effects of all the interfacial forces.

where

$$u_r = u_f - u_g, \tag{24}$$

C_D is the drag coefficient. According to Ishii and Zuber [44], the drag coefficient in Eq. (23) is generally dictated by prevailing bubble shape regime, which is classified in gas-liquid flows into three categories: viscous, distorted particle, and cap bubble. In microgravity, C_D in the distorted particle regime converges to zero because of a gravity dependence. Additionally, C_D in the cap bubble regime is not considered as it fails to satisfy the required criterion of $C_{D,dis} > C_{D,cap}$. Therefore, the relation for C_D adopted in this study is the one recommended for the viscous regime, and is given by

$$C_D = \frac{24}{\mathrm{Re}_b}\left(1 + 0.15\mathrm{Re}_b^{0.75}\right), \tag{25}$$

where

$$\mathrm{Re}_b = \frac{\rho_f |u_r| d_b}{\mu_f}. \tag{26}$$

3.1.3.5. Flowchart for the model computations. The UDF adopted in the present simulations is detailed in the flowchart depicted in Fig. 4. As the fluid enters the heated portion of the flow channel in subcooled liquid state, shear lift force plays no role at the beginning. Once phase change occurs, the algorithm identifies cells occupied by the vapor phase whose volume fraction is greater than or equal to a specific reference value of 0.5 and obtains total vapor volume within the entire domain through the summation of cells with vapor. It also sums all face areas where vapor contacts the thermally conjugated surface between the fluid and solid cells. These two values are saved into allocated memory, recalled by the UDF, and used to calculate the mean diameter of vapor every numerical iteration by dividing the total volume of vapor cells by the total surface area of vapor.

The detailed procedure for calculating the bubble collision dispersion force in the UDF is also described in the flowchart shown in Fig. 4. Since the fluid enters the heated portion of the channel in subcooled liquid state, the bubble collision dispersion force is nonexistent in the inlet region. Once phase change begins to take place, the UDF algorithm identifies cells occupied only by liquid (having zero void fraction) and loops around the identified liquid cells to calculate a volume-averaged mean liquid velocity. Using the local velocity for each vapor cell, the liquid fluctuating velocity—also termed *agitation velocity*—is calculated as the absolute difference between mean liquid velocity and local vapor velocity. The agitation velocity is saved into allocated memory and

Table 2
Averaged wall temperature for grid convergence analysis.

Case	The number of cells ($H \times W \times L_h$)	The minimum cell size, Δc [μm]	T_w [°C]
Mesh 1	46 × 36 × 572	9.4	71.01
Mesh 2	56 × 36 × 572	7.6	69.54
Mesh 3	66 × 36 × 572	6.5	68.86
Mesh 4	76 × 36 × 572	5.5	69.25

Table 3
Operating conditions employed in the CFD simulations for n-PFH flow boiling.

Test case	G (kg/m^{2}s)	P_{in} (kPa)	q'' (W/m^2)	$T_{sat,in}$ (°C)	$\Delta T_{sub,in}$ (°C)	$x_{e,in}$
1	199.9	129.5	41,406	64.5	15.4	−0.20
2		129.7	66,196	64.6	15.2	−0.20
3		133.2	116,891	65.4	15.6	−0.20
4	799.9	130.0	60,748	64.7	14.9	−0.19
5		130.4	128,964	64.8	14.8	−0.19
6		131.2	191,233	65.0	14.7	−0.19
7	2399.9	127.0	80,834	64.7	14.1	−0.18
8		127.5	177,387	65.0	13.9	−0.18
9		128.0	239,715	64.9	13.7	−0.17

recalled in the process of computing the bubble collision dispersion force, which is applied only at the interface between the liquid and vapor. To do so, the algorithm detects the liquid-vapor interface by identifying cells having a void fraction between 0 and 1. For the identified cells, agitation velocity and gradient of volume fraction of vapor, $\nabla\alpha$, are used to calculate the force, according to Eq. (21), which is incorporated as a source term in the momentum conservation equation.

3.2. Computational domain and boundary conditions

The 3D CFD model adopted in the present study accounts for actual geometric design of the flow channel, including the placement of discrete resistive heaters on the outer surface of the copper slabs. The computational domain is modeled as a rectangular channel with 5.0-mm height, 2.5-mm width, and 129.6-mm length with full consideration of the six discrete heaters on each copper slab as shown in Fig. 3(a). The total length of the domain consists of an upstream adiabatic entry length, $L_{entrance}$ = 5 mm, a heated length, L_h = 114.6 mm, and adiabatic exit length, L_{exit} = 10 mm. The width and thickness of the copper slab are 15.5 mm and 1.04 mm, respectively.

Since the accuracy of fluid flow and heat transfer predictions is considerably influenced by mesh size, a careful series of grid size iterations is undertaken down to a size below which solution convergence is ensured. The mesh used consists of 938,592 quadrilateral cells and 1030,800 nodes. As shown in Fig. 3(b), the mesh in the near-wall region is refined to Δc = 0.006-mm grid size to accurately capture key fluid flow and heat transfer characteristics, including shear stress, thermal diffusion, and vapor growth, while a coarser but uniform mesh with Δc = 0.166 mm is adopted for the core region. Grid independence and y^+ values for this domain were verified in the authors' prior studies [24,33]. Summarized in Table 2 are results of the grid convergence analysis for the case with intermediate operating conditions by means of successive refinements. As shown in the author's prior 2D work [39], a near-wall cell size below 14 mm exhibited grid-independent results. Thus, four different grids along the height of the flow channel are examined in 3D to determine the optimized mesh to capture bubble nucleation and account for near-wall latent heat transfer. It shows that asymptotic convergence of averaged wall temperature is achieved using the near-wall cell size below 7.6 mm. A cell size of 6.5 mm was therefore selected in the present study to provide desired accuracy with minimum computing time.

As indicated in Table 3, all simulations are conducted using the dielectric fluid n-PFH with nine different combinations of mass velocity and heat flux, all corresponding to double-sided heating along two opposite shorter walls (W) of the channel under ideal conditions of g/g_e = 0. The tested conditions include mass velocities from 199.9 to 2399.9 kg/m^{2}s and inlet qualities from −0.20 to −0.17. Constant heat flux based on actual power input from experiment is applied along six discrete heated regions of each heating wall corresponding to locations of the thick film resistors. A coupled heat flux condition is applied to the interface between solid and fluid cells to address conjugate heat transfer properly. The other side of the top copper wall is assigned as an adiabatic condition. Fully developed velocity profiles for the inlet boundary with turbulent intensity calculated according to $I = u'/\bar{u} = 0.16\mathrm{Re}_D^{-1/8}$ are adopted. Uniform outlet pressure, measured from the experiment, is applied to the domain's exit. A non-slip condition is applied to all surfaces, and the contact angle (estimated from vapor-solid interface to vapor-liquid interface) is set based on wall superheat evaluated from experiment. Variable time-step size ranging from 10^{-5} to 10^{-7} s is used while satisfying a global Courant number ($u\Delta t/\Delta c$) of unity for numerical stability.

4. Results and discussion

4.1. Partially developed boiling (PDB) and fully developed boiling (FDB)

As all conditions are considered in the present study are for subcooled liquid at the inlet, understanding the effects of subcooling on bubble initiation and growth, and boiling regime is essential. The liquid entering the flow channel initially undergoes single-phase liquid convection wherein the liquid's temperature increases by gaining sensible heat. Bubble initiation occurs when the wall temperature exceeds the temperature corresponding to the onset of nucleate boiling (ONB). A *subcooled boiling region* extends from the ONB location to the location where the thermodynamic equilibrium quality, x_e, reaches to zero. The subcooled boiling region can be demarcated into two sub-regions: upstream *partially developed boiling* (PDB) and downstream *fully developed boiling* (FDB). PDB is defined as a status of bubbles remaining attached to or confined to close vicinity of the heated surface due to appreciable condensation brought about by the subcooled liquid core. After the *net-vapor generation* (NVG) location, the boiling regime transitions from PDB to FDB as bubbles begin lifting off the surface and void fraction begins increasing at a much larger rate due to a de-

clining rate of condensation and an increased number of cavities activated.

Data points examined in this study are mapped in two plots proposed by Mohammed and Shah [45] to determine which boiling regime is predominant and to identify the transition from PDB to FDB. PDB and FDB can be classified via magnitudes of the following dimensionless parameters:

$$\frac{\psi}{\psi_0} = \frac{q'/\left[h_{sp}\left(T_{w,b} - T_{sat}\right)\right]}{\psi_0}, \tag{27}$$

$$\frac{\Delta T_{sub}}{\Delta T_{sat}} = \frac{T_{sat} - T_f}{T_{w,b} - T_{sat}}, \tag{28}$$

and

$$Bo = \frac{q'}{Gh_{fg}}, \tag{29}$$

where ψ is the ratio of average heat flux to single phase heat flux based on heated surface area, ψ_0 is the value of ψ corresponding to zero wall superheat, and Bo is the Boiling number. Fig. 6(a) shows that all three mass velocities with heat fluxes corresponding to 20%–22% of CHF are in the PDB region, while FDB governs the rest of the operating conditions. Notice that the laminar flow conditions yield higher values of ψ/ψ_0 for the case with the lowest mass velocity of G = 199.9 kg/m^{2}s. Data investigated in the study can be further segregated by plotting $\Delta T_{sub}/\Delta T_{sat}$ versus Bo as seen in Fig. 6(b). Here too, for cases with heat fluxes corresponding to 20–22% of CHF, no transition to FDB is observed, and PDB persists until the end of the flow channel. On the other hand, for cases with the intermediate and high heat fluxes corresponding to approximately 40% and 60%, respectively, the entire length is dominated by FDB.

4.2. Bubble behavior and hydrodynamic characteristics of subcooled flow boiling

In microgravity, absence of a body force implies flow structure is the outcome of the combined effects of inertia and surface tension. Here, experimental measurements and video analysis play primary roles in assessing the effectiveness and accuracy of the CFD model which is improved by being consolidated with additional force terms in the momentum equation. Fig. 7 presents comparisons of flow visualization images obtained via high-speed video for representative cases of a subcooled inlet during ISS experiments with predictions of the 3D CFD model. For all the simulation results presented in this study, values of the Lee mass transfer model's intensity factors are set at r_e = 100 for evaporation and r_c = 20 for condensation based on effectiveness of these values at yielding best overall agreement with experimental results for the three different mass velocities and three percentages of CHF. Both individual images from experiments and predictions illustrate instantaneous spatial tracking of interfacial behavior after a steady state is achieved. Note that with all cases having $\Delta T_{sub,}$ in the range of 13.7–15.4 °C, they can be classified as highly-subcooled as they experience subcooled flow boiling all along the heated length.

The features of PDB and FDB discussed in Section 4.1 are clearly observed in the flow visualization images. For the cases with heat fluxes corresponding to around 20% of CHF, PDB governs the entire heated length of the channel with no dramatic increase in bubble nucleation and most of the channel occupied by the subcooled bulk liquid. This is further evidenced by the fact that the exit thermodynamic equilibrium qualities corresponding to those cases are $x_{e,out}$ = −0.08, −0.15, and −0.16. Very tiny bubbles are generated on the walls and preserve their size as they slide along because of the strong condensation effects provided by the highly subcooled bulk flow. It is clearly observed that these small bubbles tend to remain attached to both walls. Because of zero body force, vapor bubble nucleation is governed mostly by shear-lift and drag.

Larger bubbles are formed along both walls at higher heat fluxes corresponding to around 40% CHF. Some of the bubbles in the cases of G = 199.9 kg/m^{2}s and 799.9 kg/m^{2}s are sheared off the heated wall, but they do not fully condense in the bulk liquid due to weakened condensation effects in the FDB region as evaluated in Figs. 6(a) and (b). For the case of G = 2399.9 kg/m^{2}s, bubbles are also formed, but remain close to the walls because of strong liquid drag rather than bulk subcooling. An increase in void fraction is noticeable after increasing heat flux to around 60% of CHF. Much larger bubbles are pinched, deformed, and migrated toward the channel core region, becoming large, elongated bubbles downstream for both G = 199.9 kg/m^{2}s and 799.9 kg/m^{2}s. However, unlike those two cases, massive vapor generation is not seen and most bubbles maintain proximity to the walls at G = 2399.9 kg/m^{2}s.

The two-phase flow structures predicted by the enhanced computational approach are captured in Fig. 7 and compared to the images from experiment. Simulation results were instantaneously captured after the computation reached steady state. For each mass velocity, the simulations effectively capture the monotonic increase in the amount of evaporation with increasing heat flux and culmination with significant vapor accumulation along the walls downstream. In particular, for the case of q'' = 60% of CHF (except the case of G = 2399.9 kg/m^{2}s), bubble nucleation in the simulations commences near the leading edge of the heated length and discrete wavy vapor blankets on the opposite heated walls begin to grow from the middle of the channel length, which match flow visualizations from experiment. At the highest mass velocity, relatively tiny bubbles are formed and stay close to the heated walls compared to the other mass velocities of G = 199.9 kg/m^{2}s and 799.9 kg/m^{2}s for similar heat flux percentages of CHF. This is because highly subcooled liquid occupies the largest portion of the cross-section area, which is proven by the fact that the $x_{e,out}$ is still −0.11.

More details of the dynamic behavior of flow boiling are illustrated by sequential images captured from the simulations, which are shown in Figs. 8(a)–(c), wherein individual images in each sequence are separated by 5 ms. Shown for each of the mass velocities of G = 199.9, 799.9, and 2399.9 kg/m^{2}s are visualizations for heat fluxes corresponding to around 40% and 60% of CHF. The flow visualizations corresponding to around 20% of CHF are excluded since single-phase liquid convective flow governs these conditions and only a few minute bubbles are produced on the heated walls as a result of subcooled boiling within the PDB region. The exact values of operating conditions including heat fluxes are indicated in Figs. 8(a)–(c).

For all three mass velocities, the bubbly flow regime is predominant along the heated length at around 40% of CHF, and bubble sizes become increasingly smaller with increasing G. The flow regimes from simulations for G = 199.9 and 799.9 kg/m^{2}s exhibit appreciable changes as the heat flux is increased from about 40% to 60% of CHF, however, changes are less prevalent for G = 2399.9 kg/m^{2}s.

As seen in Fig. 8(a), at G = 199.9 kg/m^{2}s and 35% of CHF, bubble nucleation occurs upstream and detached bubbles begins to lift off towards the bulk liquid core. Some of the bubbles flowing downstream in the bulk region merge with other bubbles being pinched off from the walls. Due to bubble coalescence with neighboring bubbles, tiny bubbles grow into larger, oblong bubbles downstream. The flow regime transitions from bubbly to slug/churn with increasing heat flux. At the higher q'' = 11.7 W/cm^2 (corresponding to 62% of CHF), bubble nucleation takes place at the leading edge of the heated walls, forming wavy vapor layers along the walls. The waviness is manifest by formation of crest and trough

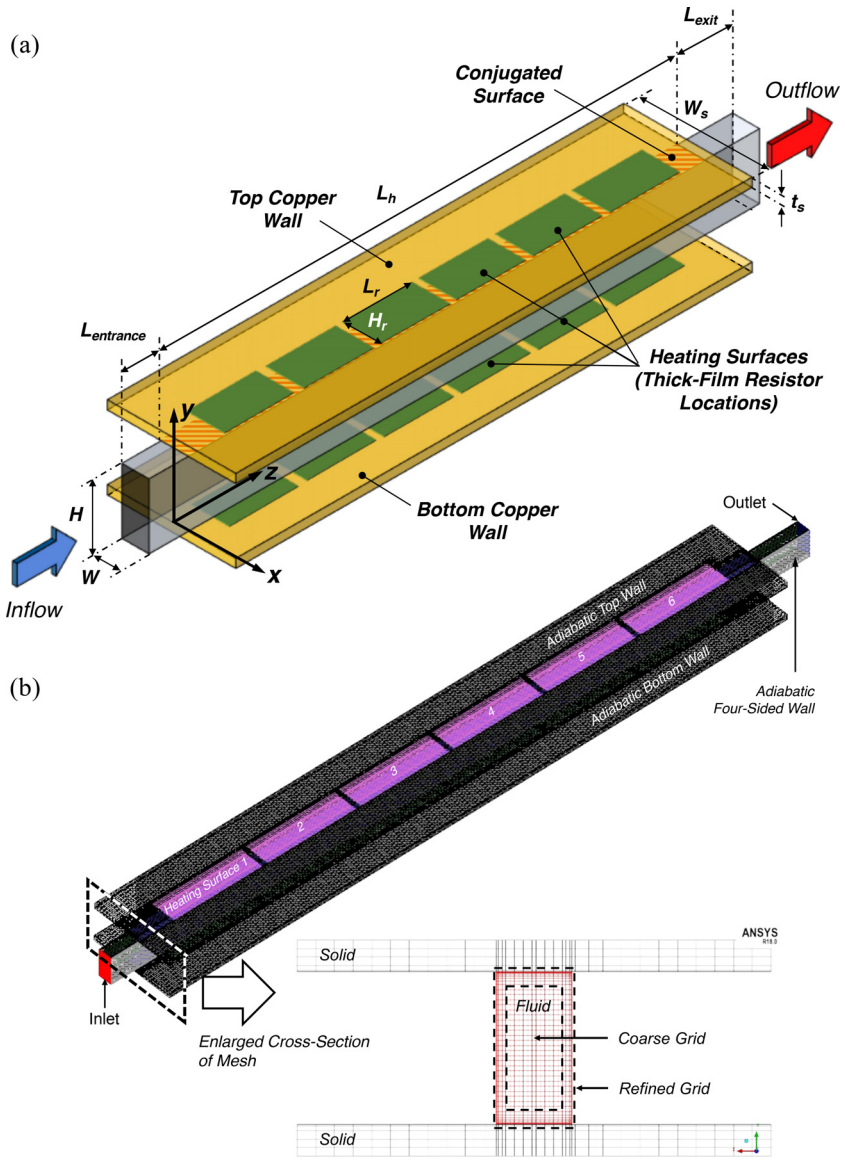

Fig. 5. (a) Schematic of 3D computational geometry. (b) Mesh configuration in full domain and cross-section area.

regions toward the middle of the heated length, with crests from the opposite walls ultimately merging farther downstream, forming elongated bubbles that engulf almost the entire cross section.

In Figs. 8(b) and (c), corresponding to G = 199.9 and 799.9 kg/m^{2}s, respectively, tiny and discrete bubbles are generated along the heated walls at q'' = 12.9 and 17.7 W/cm^2, corresponding to 42% and 43% of CHF, respectively. Here, bubble growth is rather small, and the bubbles tend to stay close to the walls. This is because: (1) ability of the liquid to maintain its subcooling is considerable at higher mass flow rates, (2) bubble growth is limited within the thin thermal wall boundary layers, (3) bubble shear lift is relatively small due to small projected area of the small bubbles, and (4) high inertia of the liquid prevents tiny bubbles from moving toward the bulk region. Like Fig. 8(a), due to an increased evaporation rate at the higher q'' = 19.1 W/cm^2, a transition to slug/churn flow is observed for the case of G = 799.9 kg/m^{2}s. Here, some of the bubbles detach from crests of the vapor layers, migrating towards the core region and causing coalescence of vapor layers from the opposite walls into large, elongated bubbles farther downstream. The simulations also capture bubble nucleation occurring downstream within the liquid layer trapped between the elongated bubbles and the walls.

On the other hand, Fig. 8(c) shows, for G = 2399.9 kg/m^{2}s, the bubbly flow regime is maintained along the entire heated length despite the increasing void fraction at the higher heat flux, and, for both heat fluxes, a significant portion of the channel's cross section is occupied by liquid and discrete bubbles are constrained near the walls.

Also, important to understanding interfacial behavior within the channel are distributions of void fraction within the channel's cross-section at different axial locations. It is important here to emphasize the symmetries in both inlet velocity profile and heat flux applied to the two heated walls. This means these symmetries will also be reflected in predictions of vapor generation within the channel. Predictions are provided in Fig. 9 in the form of transverse void profiles at different axial locations along the channel for each of the three mass velocities. Time-averages for the void fraction are achieved over a period of one second. Notice how the void fraction profiles resemble those typical of bubbly flow with a subcooled liquid core. The profile for each mass velocity starts with zero distribution at the upstream location, meaning no vapor has yet

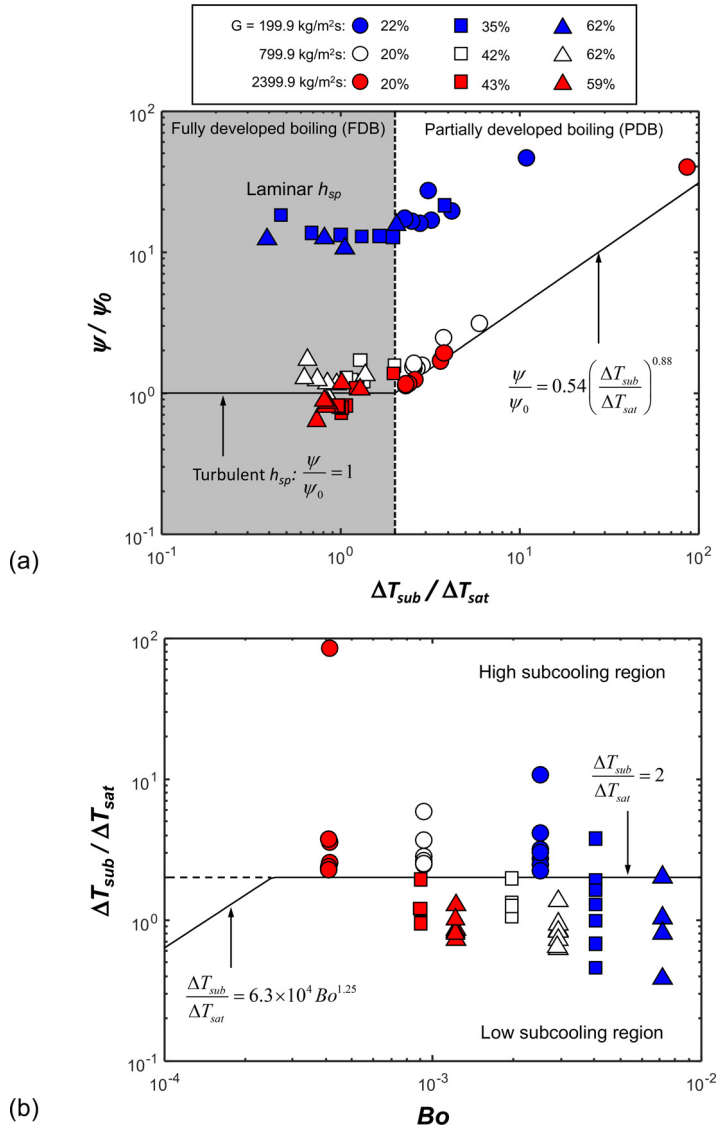

Fig. 6. Data classification into partially developed boiling (PDB) and fully developed boiling (FDB) regions according to (a) ratio of dimensionless heat transfer rate, Ψ/Ψ_0 versus $\Delta T_{sub}/\Delta T_{sat}$, and (b) $\Delta T_{sub}/\Delta T_{sat}$ versus Boiling number, *Bo*.

been generated. This is followed at the second axial location with peak void in close proximity to the walls, in contrast with miniscule void near the centerline. This is indicative of a bubble layer residing near the wall, with liquid occupying most of the channel core. For the lowest and middle mass velocities, G = 199.94 and 799.97 kg/m^{2}s, respectively, Fig. 9 shows further penetration of the vapor layer towards the centerline at the third and fourth axial locations, which is the outcome of bubble growth and coalescence promoted by gradual warming of core liquid. There are important differences between the void distributions for the lowest and middle mass velocities on one hand and those for the highest mass velocity. For the highest mass velocity (G = 2399.9 kg/m^{2}s), near-wall peaks in the void profile increase while maintaining zero value across much of the core, the latter is the result of greater sensible energy content in the subcooled liquid at high mass velocities. Confinement of the bubble layer to the wall region is also the result of greater liquid inertia for the highest mass velocity.

Local streamwise velocity profiles are also provided to highlight the interrelationship between void fraction and vapor-liquid mixture velocity. Predictions are shown in Fig. 10 for the three mass velocities, each including velocity profile trends for three axial locations of z = 22.7, 57.3, and 91.9 mm and three percentages of CHF. The profile data are time-averaged after steady-state. For the lowest mass velocity of G = 199.9 kg/m^{2}s, Fig. 10(a), the upstream region of z = 22.7 mm shows limited y-direction profile distortions because of minimal bubble generation within the PDB region and most of the bubbles remaining attached to the heated walls. The distortions are also limited for 22% of CHF regardless of axial location. This is the outcome of PDB spanning much of the heated length. Distortion severity increases significantly with increases in% of CHF and axial location because of intensified, larger-scale bubble activity, including more appreciable bubble growth, departure, and coalescence to larger vapor bubbles. Also, as already shown earlier in Fig 9(a), void fraction for G = 199.9 kg/m^{2}s increases appreciably with the increases in wall heating (especially for q″ = 62% of CHF) as well as with axial location. This culminates in significant flow acceleration with increasing heat flux and axial location, with large, elongated bubbles showing greatest effect towards y = 0. For G = 799.9 kg/m^{2}s, Fig. 10(b), two obvious differences from Fig. 10(a) trends are readily apparent. Because of smaller void fraction (see Fig. 9(b)), both the profile distortions and flow acceleration effects are attenuated. These trends are even more evident

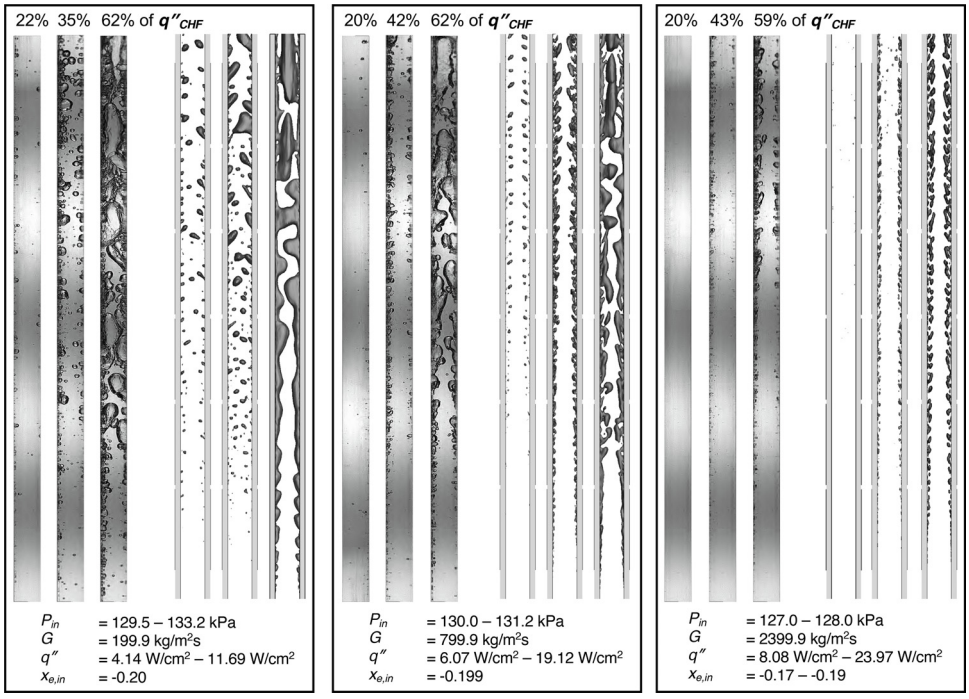

Fig. 7. Comparisons of experimentally captured flow visualizations with computational predictions for three different mass velocities and heat fluxes corresponding to similar percentages of CHF.

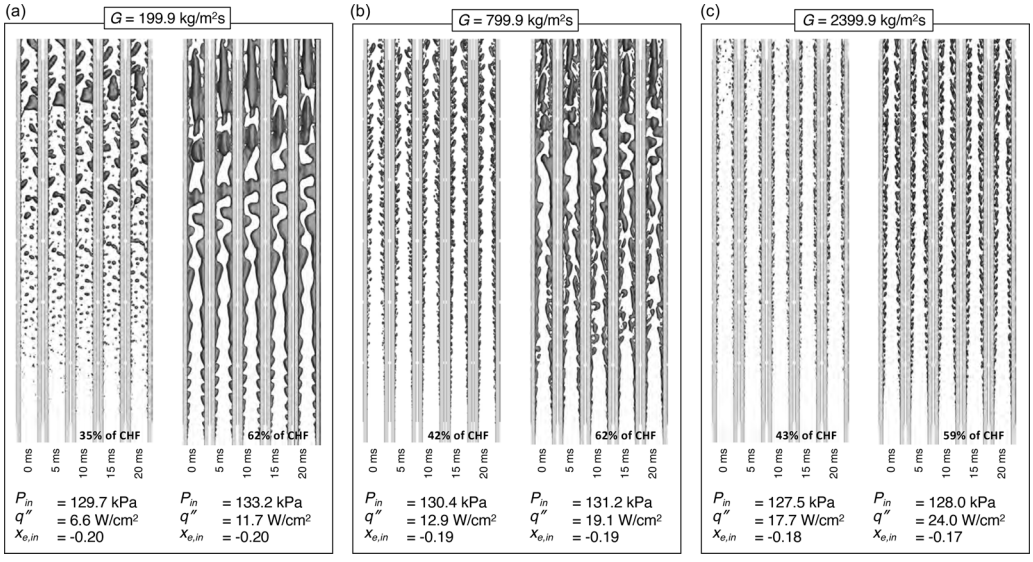

Fig. 8. Flow visualizations from simulations for (a) $G = 199.9$ kg/m^{2}s, (b) $G = 799.9$ kg/m^{2}s, and (c) $G = 2399.9$ kg/m^{2}s.

for $G = 2399.9$ kg/m^{2}s, Fig. 10(c), where miniscule vapor production (see Fig. 9(c)) precipitates negligible distortions or flow acceleration even for 59% of CHF and $z = 91.9$ mm.

4.3. Flow boiling heat transfer characteristics

Fig. 11 shows comparisons of measured and predicted heated wall temperature variations along the heated length for the three mass velocities and heat fluxes corresponding to approximately 20%, 40%, and 60% of CHF. The temperatures are measured experimentally by the thermocouples embedded into the copper slab at $z = 5.4$, 22.7, 40.0, 57.3, 74.6, 91.9, and 109.2 mm. The predicted temperatures are calculated within the solid cells at the exact depth of the thermocouple, then time-averaged after a steady state is reached. Several important observations are apparent from these plots. First, both measured and predicted wall temperatures are fairly uniform along the heated length due to the latent heat transfer, albeit with slightly lower values in the entrance and exit regions. The lower temperatures upstream are attributed to development of a thin upstream thermal boundary layer where single-phase cooling is appreciable and two-phase cooling is not fully developed, whereas the lower temperatures downstream are the outcome of improved heat transfer resulting from fluid acceleration. Those upstream and downstream temperature trends are also captured in the CFD simulations. For cases corresponding to 20% and 40% of CHF, predicted temperature shows good agreement with measurement, but noticeable deviations are detected from the cases with the highest q''. Overall, maximum and minimum devia-

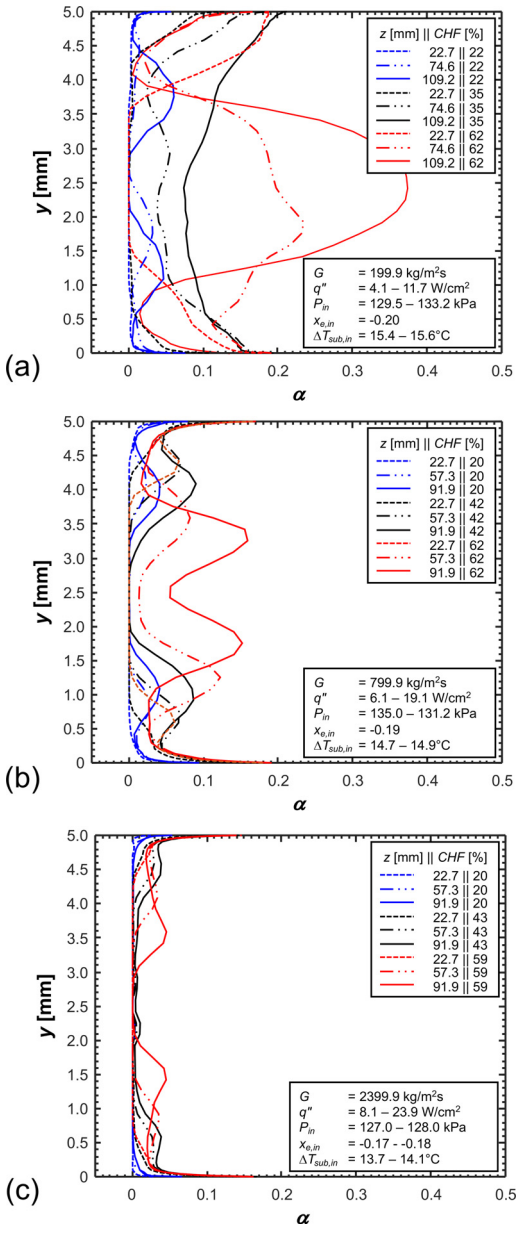

Fig. 9. Time-averaged local void fraction profiles between the heated walls for (a) G = 199.9 kg/m^{2}s, (b) G = 799.9 kg/m^{2}s, and (c) G = 2399.9 kg/m^{2}s.

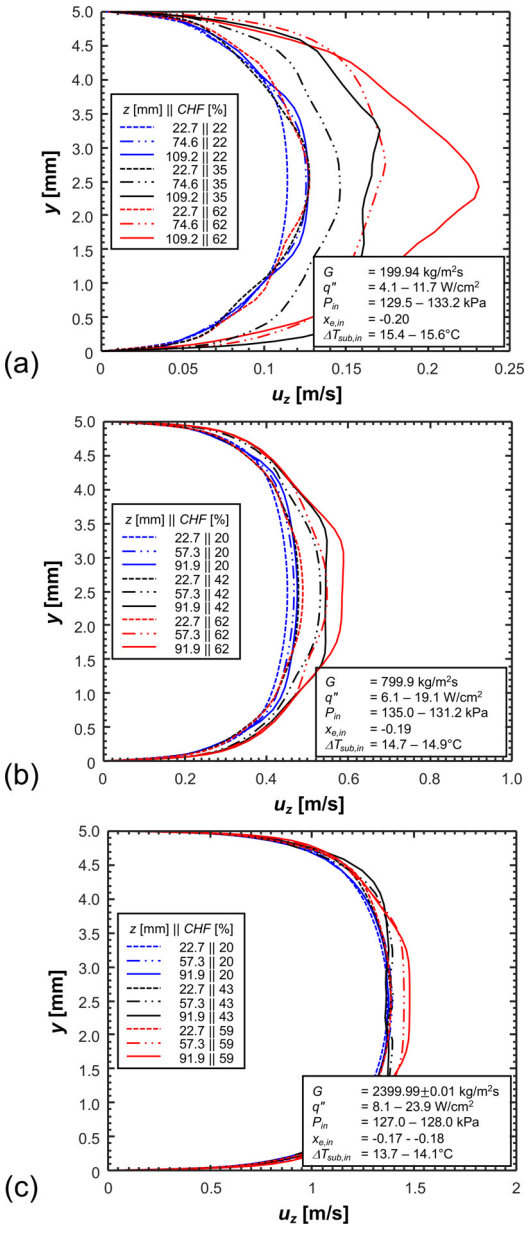

Fig. 10. Time-averaged velocity profiles between the heated walls for G = (a) 199.9 kg/m^{2}s, (b) 799.9 kg/m^{2}s, and (c) 2399.9 kg/m^{2}s.

tions between measured and predicted $T_{w,avg}$ for all operating conditions of this study are 9.17 and 0.02 °C, respectively, with the measured showing up to 16.64 °C superheat above saturation temperature compared to 20.36 °C for the predicted. Maximum deviation is detected for G = 799.9 kg/m^{2}s and q'' = 191,233 W/m^2. Some of the deviations in Fig. 11 can be attributed to limitations of the CFD method, especially an apparent inability to maintain the bubbly flow regime at high heat fluxes. As shown in the flow visualization comparison of Fig. 7, for the cases of G = 199.9 and 799.9 kg/m^{2}s with the highest q'', small discrete bubbles more easily turn into larger bubbles or vapor layers in simulations. In experiments, however, discrete bubbles maintain their formation even though they are touching together, perhaps because of a tendency to maintain their minimum free surface energy. The limitation of the CFD model is rooted in the tracking and reconstruction of interfaces based on void fraction only, which causes larger bubbles to be easily generated once neighboring bubbles meet, leading to a quick transition from bubbly to other evolved flow regimes. Another factor for the deviation is related to details of bubble-induced turbulence, which stems from inherent limitations of the numerical and mathematical algorithms when computing liquid velocities around bubbles and the use of volume-fraction-averaged physical properties at mixture cells to avoid sharp discontinuities across the interface that cannot be numerically differentiated. Overall, despite these deviations, Fig. 11 shows evidence the CFD model provides fairly good predictions.

Fig. 12 compares axial variations of numerically computed and analytically calculated average fluid temperature, T_m. Here, computed temperature from the simulations is a volume-weighted average over the cross-sectional area, while the analytically estimated temperature is based on inlet and outlet measured fluid temperature and pressure. The analytically calculated values account for axial variations of saturation temperature resulting from pressure drops across the heated portion of the channel, which is assumed to be linear. Details are discussed in Section 2. Both calculated thermodynamic equilibrium quality and fluid temper-

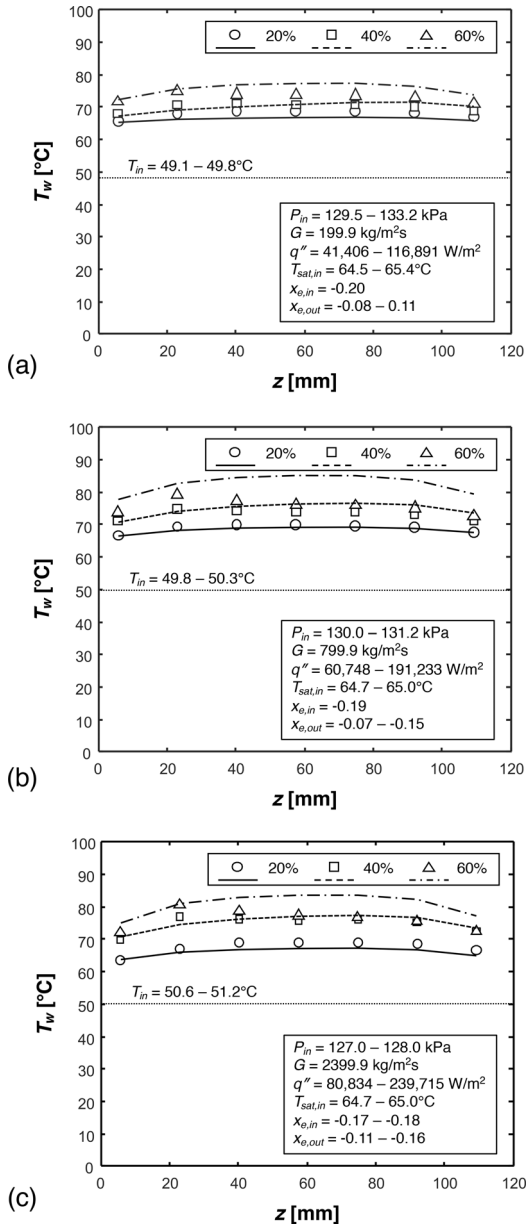

Fig. 11. Comparisons of measured and predicted axial variations of heated wall temperature for (a) G = 199.9 kg/m²s, (b) G = 799.9 kg/m²s, and (c) G = 2399.9 kg/m²s.

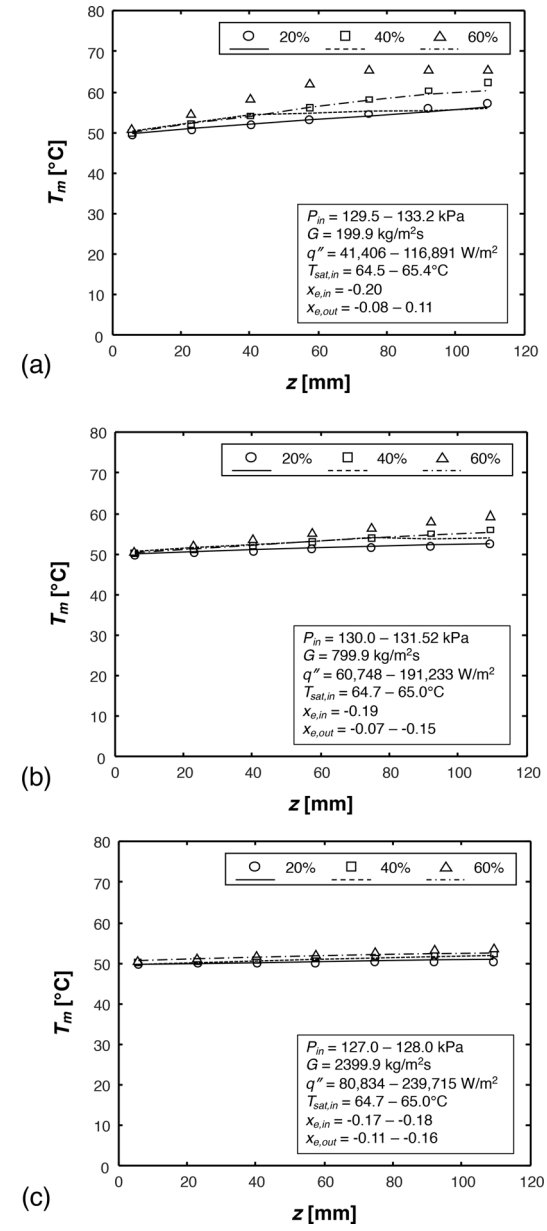

Fig. 12. Comparisons of measured and predicted axial variations of mixture temperature for (a) G = 199.9 kg/m²s, (b) G = 799.9 kg/m²s, and (c) G = 2399.9 kg/m²s.

ature are determined from a simple energy balance considering heat input from the heated walls. Calculation of fluid temperature upstream of the location where thermodynamic equilibrium quality, x_e, equals zero is based on sensible heat gain. But, for downstream locations where $0 < x_e < 1$, local fluid temperature is set equal to saturation temperature corresponding to local pressure. As shown in Fig. 12, the computed fluid temperature in simulations reflects the expected nearly linear trend in the upstream subcooled region ($x_e < 0$), followed by a flatter, near saturated temperature where $x_e > 0$. Maximum deviation detected from the case of G = 199.9 kg/m²s and the highest q'' is 7.0 °C at the fifth measurement location of z = 74.6 mm where fluid temperature is determined by the local saturation temperature as $x_e > 0$. This can be explained by the fact that the analytical estimations are based entirely on idealized thermodynamic equilibrium quality assumptions, whereas the computed values account for realistic non-equilibrium effects. Excepting this case, Fig. 12 shows good agreement between numerically computed and analytically calculated fluid temperatures, especially in the inlet and outlet regions.

Fig. 13 shows cross-sectional profiles of numerically computed fluid mixture temperature for mass velocities of G = 199.9, 799.9, and 2399.9 kg/m²s, each including profile trends for three axial locations of z = 22.7, 57.3, and 91.9 mm and three percentages of CHF. As discussed earlier, the profile data are time-averaged after steady-state. Similar to the velocity profiles presented in Fig. 10, fluid mixture temperature profile gradually develops with distance due, for upstream locations and low wall heating, mostly to single-phase liquid thermal boundary layer development created from diffusion and advection from the heated walls, and for downstream locations and high wall heating, to increases in core temperature brought about by the vapor production. For the lowest mass velocity of G = 199.9 kg/m²s, Fig. 13(a), fluid temperature in the core region at z = 22.7 mm is highly subcooled regardless of heat flux. But at z = 109.2 mm, with significant vapor production, especially for 62% of CHF, the core fluid exhibits a substantial increase in

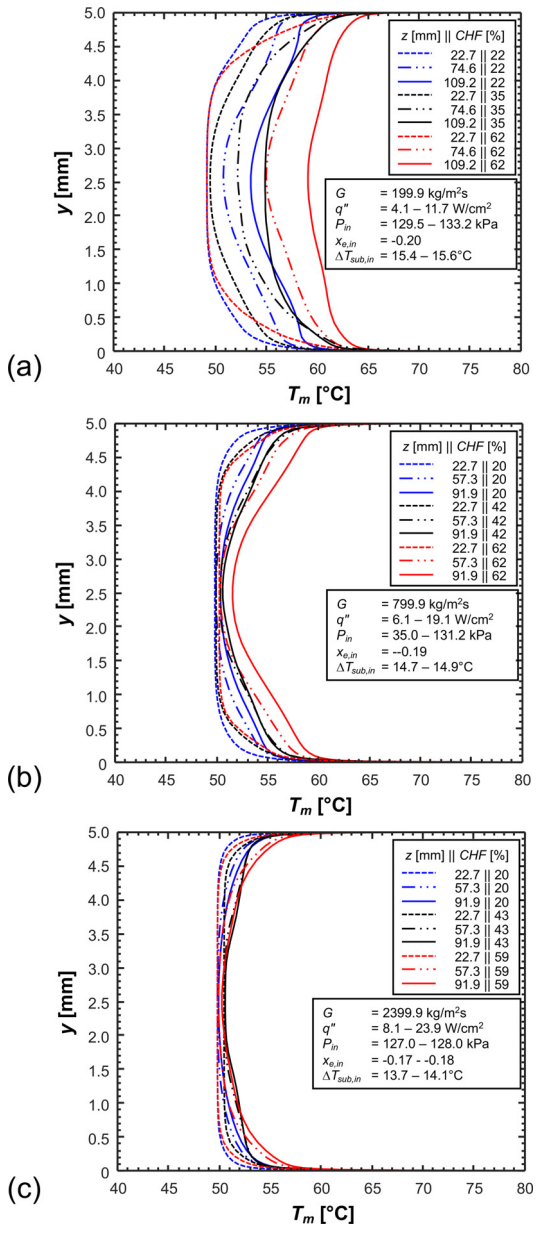

Fig. 13. Time-averaged mixture temperature profiles between the heated walls for G = (a) 199.9 kg/m^{2}s, (b) 799.9 kg/m^{2}s, and (c) 2399.9 kg/m^{2}s.

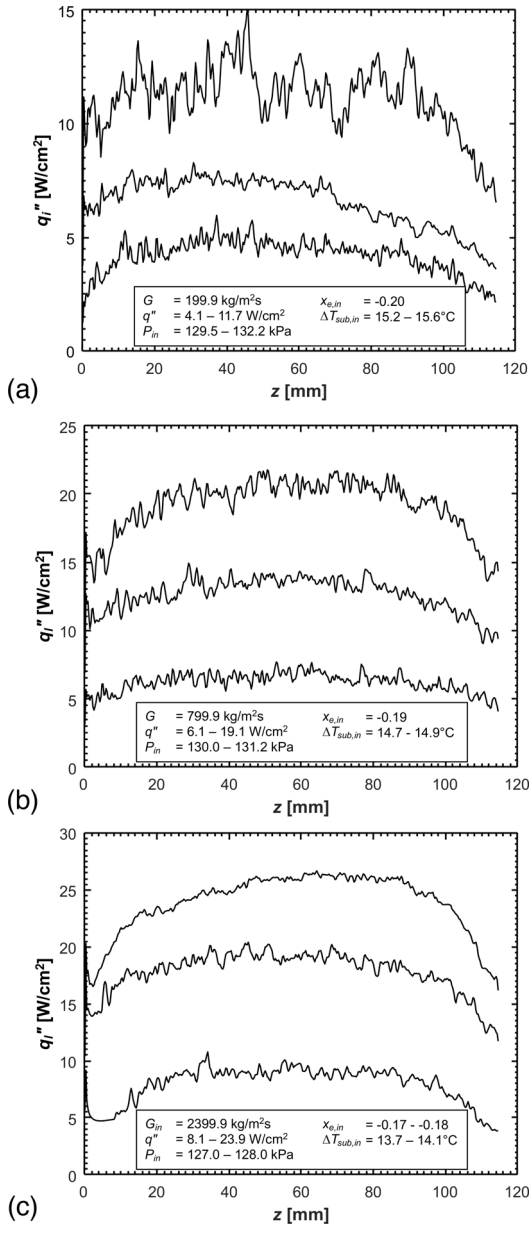

Fig. 14. Axial variations of computed surface heat flux at copper-fluid interface for (a) G = 199.9 kg/m^{2}s, (b) G = 799.9 kg/m^{2}s, and (c) G = 2399.9 kg/m^{2}s.

temperature. Note that, even at this high heating level and downstream location, the mixture temperature is still below saturation because bulk subcooled liquid is prevalent. For G = 799.9 kg/m^{2}s, Fig 13(b), decreased bubble nucleation and growth within the thermal boundary layer is reflected by reduced profile variations regardless of wall heating or axial location. For G = 2399.9 kg/m^{2}s, Fig. 13(c), the changes in fluid temperature profile with heating and axial location are attenuated even further.

Fig. 14 shows predicted axial variations of wall surface heat flux. Values for one of the two heated walls are time- and space-averaged across the transverse x-direction. The surface heat flux, q''_i, is defined as that passing through the interface from the copper to fluid and is different from the constant heat flux q" indicated in the previous plots. The surface heat flux is a dependent variable influenced by relative contributions of sensible and latent heating and, therefore, by all details of bubble nucleation, growth, departure, and coalescence, and liquid replenishment. Notice that heating along the heated wall is concentrated around regions corresponding to locations of the thick film resistors, so q''_i is small until the axial location corresponding to the upstream edge of the most upstream resistive heater, z = 5.85 mm. Nonetheless, for all three mass velocities, q''_i shows an uptick at z = 0, stemming from the initiation of a very thin thermal boundary layer near the inlet and convective single phase liquid cooling. This is followed shortly downstream by a decrease in q''_i, the outcome of gradual thickening of the boundary layer. Shortly thereafter, q''_i begins to increase as bubbles begin to nucleate within the upstream region, first sparsely, and then more aggressively. It seems that q''_i is rather flat in the middle of the heated length due to the nucleate boiling regime's dominance, but with some severe fluctuations observed at the highest heat flux conditions for the cases of G = 199.9 and 799.9 kg/m^{2}s due to axial propagation of the vapor layer and wetting fronts. Moreover, the downstream decrease in q''_i is attributed to localized vapor blanketing upon the heated wall as well as the existence of a 5.85-mm unheated downstream length beginning at the downstream edge of the most downstream

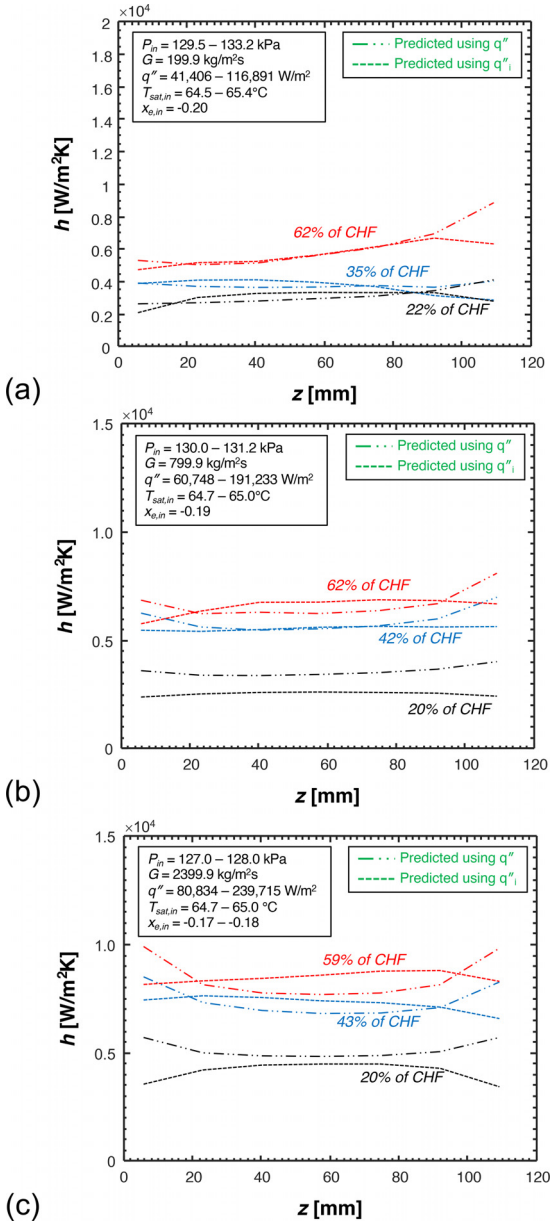

Fig. 15. Axial variations of heat transfer coefficient for (a) G = 199.9 kg/m^{2}s, (b) G = 799.9 kg/m^{2}s, and (c) G = 2399.9 kg/m^{2}s.

resistive heater (z = 108.75 mm). For the highest mass velocity, G = 2399.9 kg/m^{2}s, high shear and drag forces, and more effective bulk flow condensation cause the upstream increase in vapor void to subside beginning more upstream than for the two lower mass velocity cases, culminating in rather flat profiles spanning much of the middle portion of the heated length.

Fig. 15 shows axial variations of predicted heat transfer coefficient, h, for G = 199.9, 799.9, and 2399.9 kg/m^{2}s and heat fluxes ranging from around 20% to 60% of CHF. The temperature data used here are time-averaged over a period of one second after reaching steady-state. When computing local wall-to-fluid temperature difference, the local fluid temperature is averaged over the cross-sectional area. Because of differences between axially uniform q'' and axially changing q''_i, different values for h are realized. For G = 199.9 kg.m^{2}s, Fig. 15(a), differences in computed h values are small over the middle portion of the heated length, but noticeable both upstream and downstream where Fig. 14(a) showed appreciable decline in q''_i. Similar differences are manifest for G = 799.9 kg.m^{2}s, Fig. 15(b), and G = 2399.9 kg.m^{2}s, Fig. 15(c), albeit with greater overall deviation due in part to increased deviation between measured and predicted wall temperatures as shown earlier in Fig. 11.

Overall, the present computational model shows good accuracy in predicting both interfacial behavior and heat transfer data, albeit with deviations that increase with increasing heat flux. This is despite several limitations of the model that were discussed earlier. The authors are aiming to further improve predictions in future work by replacing the VOF model with the Coupled Level Set Volume of Fluid (CLSVOF) model, which capitalizes upon VOF's accuracy in calculating interfacial mass transfer, and the Level Set (LS) model's ability to calculate surface tension force more accurately and therefore improve tracking of sharp interfaces.

Conclusions

The present study focused on the use of Computational Fluid Dynamics (CFD) to predict near-saturated flow boiling of n-PFH in microgravity. The computational method used provided detailed 3D predictions of interfacial behavior and heat transfer characteristics along a rectangular channel heated along two opposite walls. The CFD model is based on the multiphase volume-of-fluid (VOF) model, which is combined with appropriate phase change and turbulence models and modified and improved with addition of forces associated with surface tension, drag, shear-lift on bubbles, and bubble collision dispersion; the model also accounts for conjugate heat transfer along the heating walls. Model validation is achieved by comparing predictions to experimental wall temperature measurements and high-speed video images captured from experiments that were conducted onboard the International Space Station (ISS). This study represents the first effort to predict the ISS data. Key findings from the study are as follows:

1) For all three mass velocities considered, G = 199.9, 799.9, and 2399.9 kg/m^{2}s, bubble nucleation persisted along the heated length at heat fluxes corresponding to around 20% and 40% of CHF. For the two lower mass velocities, increasing the heat flux to around 60% of CHF culminated in significant bubble coalescence and formation of large elongated bubbles and vapor layers, especially downstream. On the other hand, high flow inertia at G = 2399.9 kg/m^{2}s greatly reduced both bubble growth and coalescence for all heat fluxes.
2) Overall, the present computational model shows good accuracy in predicting both the interfacial behavior and heat transfer data. For each of the three mass velocities and three heat fluxes considered, both measured and predicted wall temperatures are fairly uniform along the heated length, albeit with slightly lower values in the entrance and exit regions. The lower temperatures upstream are attributed to development of a thin upstream thermal boundary layer where single-phase cooling is appreciable and two-phase cooling is not fully developed, whereas the lower temperatures downstream are the outcome of improved heat transfer resulting from fluid acceleration.
3) The CFD simulations are highly effective at enabling the prediction of transport parameters vitally important to understanding evolution of the boiling flow but not possible from experiment, such as cross-sectional profiles of void fraction, fluid velocity, and mixture temperature.
4) Calculation of heat transfer coefficient is dependent on the heat flux boundary adopted along the heating walls, using either local heat flux passing through the copper-fluid interface or constant heat flux. Predicted heat transfer coefficients show good agreement along most of the heated length excepting the regions upstream of the copper slab's most upstream resis-

tive heater and downstream of the most downstream resistive heater.(Eqn (1)-20, 22, 24-29, Fig. 5)

Declaration of Competing Interest

The authors declare that they have no known competing financial interests or personal relationships that could have appeared to influence the work reported in this paper.

Data Availability

The data that has been used is confidential.

Acknowledgment

The authors are grateful for financial support provided by the National Aeronautics and Space Administration (NASA) under Grant No. 80NSSC22K0328.

References

[1] T.J. LaClair, I. Mudawar, Thermal transients in a capillary evaporator prior to the initiation of boiling, Int. J. Heat Mass Transf. 43 (2000) 3937–3952.
[2] T.M. Anderson, I. Mudawar, Microelectronic cooling by enhanced pool boiling of a dielectric fluorocarbon liquid, J. Heat Transf. 111 (1989) 752–759.
[3] I. Mudawar, R.A. Houpt, Mass and momentum transport in smooth falling liquid films laminarized at relatively high Reynolds numbers, Int. J. Heat Mass Transf. 36 (1993) 3437–3448.
[4] I. Mudawar, D.E. Maddox, Enhancement of critical heat flux from high power microelectronic heat sources in a flow channel, J. Electron. Packag. 112 (1990) 241–248.
[5] S. Mukherjee, I. Mudawar, Pumpless loop for narrow channel and micro-channel boiling, J. Electron. Packag. 125 (2003) 431–441.
[6] M.E. Johns, I. Mudawar, An ultra-high power two-phase jet-impingement avionic clamshell module, J. Electron. Packag. 118 (1996) 264–270.
[7] W.P. Klinzing, J.C. Rozzi, I. Mudawar, Film and transition boiling correlations for quenching of hot surfaces with water sprays, J. Heat Treat. 9 (1992) 91–103.
[8] M.K. Sung, I. Mudawar, Single-phase and two-phase heat transfer characteristics of low temperature hybrid micro-channel/micro-jet impingement cooling module, Int. J. Heat Mass Transf. 51 (2008) 3882–3895.
[9] M. Saito, N. Yamaoka, K. Miyazaki, M. Kinoshita, Y. Abe, Boiling two-phase flow under microgravity, Nucl. Eng. Des. 146 (1994) 451–461.
[10] Y. Ma, J.N. Chung, An experimental study of critical heat flux (CHF) in microgravity forced-convection boiling, Int. J. Multiphase Flow 27 (2001) 1753–1767.
[11] J. Zhao, Two-phase flow and pool boiling heat transfer in microgravity, Int. J. Multiphase Flow 36 (2010) 135–143.
[12] H. Zhang, I. Mudawar, M.M. Hasan, Flow boiling CHF in microgravity, Int. J. Heat Mass Transf. 48 (2005) 3107–3118.
[13] L. Galbiati, P. Andreini, Flow pattern transition for horizontal air-water flow in capillary tubes. A microgravity “equivalent system” simulation, Int. Commun. Heat Mass Transfer 21 (1994) 461–468.
[14] A. Georgoulas, M. Andredaki, M. Marengo, An enhanced VOF method coupled with heat transfer and phase change to characterise bubble detachment in saturated pool boiling, Energies 10 (2017) 272.
[15] A. Dhruv, E. Balaras, A. Riaz, J. Kim, A formulation for high-fidelity simulations of pool boiling in low gravity, Int. J. Multiphase Flow 120 (2019) 103099.
[16] S. Banerjee, Y. Lian, Y. Liu, M. Sussman, A new method for estimating bubble diameter at different gravity levels for nucleate pool boiling, J. Heat Transf. 144 (2022) 021601.
[17] I. Chakraborty, B. Ray, G. Biswas, F. Durst, A. Sharma, P.S. Ghoshdastidar, Computational investigation on bubble detachment from submerged orifice in quiescent liquid under normal and reduced gravity, Phys. Fluids 21 (2009) 062103.
[18] T.-.H. Yi, Z.-.S. Lei, J.-.F. Zhao, Numerical investigation of bubble dynamics and heat transfer in subcooling pool boiling under low gravity, Int. J. Heat Mass Transf. 132 (2019) 1176–1186.
[19] K. Guo, F. Chang, H. Li, Application of a magnetic field in saturated film boiling of a magnetic nanofluid (MNF) under reduced gravity, Energies 14 (2021) 634–658.
[20] G. Li, X. Fang, Numerical simulation on the boiling flow patterns of Al_2O_3-water nanofluid in micro/minichannel under different hypergravity levels and directions, Int. J. Aerospace Eng. 2021 (2021) 1–12.
[21] J. Wang, Y. Li, L. Wang, S. Xia, J. Ren, H. Mao, Y. Xu, Numerical investigation on subcooled pool film boiling of liquid hydrogen in different gravities, Int. J. Hydrog. Energy 46 (2021) 2646–2657.
[22] Y. Zheng, H. Chang, Y. Qiu, C. Duan, J. Chen, H. Chen, S. Shu, Prediction of liquid hydrogen flow boiling critical heat flux condition under microgravity based on the wall heat flux partition model, Int. J. Hydrog. Energy 45 (2020) 7141–7150.
[23] M. Bahreini, A. Ramiar, A.A. Ranjbar, Numerical simulation of subcooled flow boiling under conjugate heat transfer and microgravity condition in a vertical mini channel, Appl. Therm. Eng. 113 (2017) 170–185.
[24] J. Lee, I. Mudawar, M.M. Hasan, H.K. Nahra, J.R. Mackey, Experimental and computational investigation of flow boiling in microgravity, Int. J. Heat Mass Transf. 183 (2022) 122237.
[25] D. Jacqmin, Calculation of two-phase Navier–Stokes flows using phase-field modeling, J Comput Phys 155 (1999) 96–127.
[26] N.D. Katopodes, Free-Surface Flow: Computational Methods, Butterworth-Heinemann, 2018.
[27] V.S. Devahdhanush, I. Mudawar, H.K. Nahra, R. Balasubramaniam, M.M. Hasan, J.R. Mackey, Experimental heat transfer results and flow visualization of vertical upflow boiling in Earth gravity with subcooled inlet conditions – In preparation for experiments onboard the International Space Station, Int. J. Heat Mass Transf. 188 (2022) 122603.
[28] E.W. Lemmon, M.L. Huber, M.O. McLinden, NIST standard reference database 23, reference fluid thermodynamic and transport properties (REFPROP), Version. 9 (2010).
[29] W.H. Lee, A pressure iteration scheme for two-phase flow modeling, in: Multiphase transport: Fundamentals, Reactor safety, Applications, 1980, pp. 407–432.
[30] J.U. Brackbill, D.B. Kothe, C. Zemach, A continuum method for modeling surface tension, J. Comput. Phys. 100 (1992) 335–354.
[31] K.K. So, X.Y. Hu, N.A. Adams, Anti-diffusion method for interface steepening in two-phase incompressible flow, J. Comput. Phys. 230 (2011) 5155–5177.
[32] ANSYS FLUENT Theory Guide, ANSYS Inc., Canonsburg, PA, 2009.
[33] J. Lee, L.E. O’Neill, I. Mudawar, 3-D computational investigation and experimental validation of effect of shear-lift on two-phase flow and heat transfer characteristics of highly subcooled flow boiling in vertical upflow, Int. J. Heat Mass Transf. 150 (2020) 119291.
[34] R.W. Schrage, A Theoretical Study of Interphase Mass transfer, in: a Theoretical Study of Interphase Mass Transfer, Columbia University Press, 1953.
[35] I. Tanasawa, in: Advances in Condensation Heat transfer, in: Advances in Heat Transfer, Elsevier, 1991, pp. 55–139.
[36] F. Gibou, L. Chen, D. Nguyen, S. Banerjee, A level set based sharp interface method for the multiphase incompressible Navier–Stokes equations with phase change, J. Comput. Phys. 222 (2007) 536–555.
[37] M. Magnini, J.R. Thome, Computational study of saturated flow boiling within a microchannel in the slug flow regime, J. Heat Transf. 138 (2016) 021502.
[38] Y.-J. Chen, K. Ling, H. Ding, Y. Wang, S.-.Q. Jin, W.-.Q. Tao, 3-D numerical study of subcooled flow boiling in a horizontal rectangular mini-channel by VOSET, Int. J. Heat Mass Transf. 183 (2022) 122218.
[39] J. Lee, L.E. O’Neill, S. Lee, I. Mudawar, Experimental and computational investigation on two-phase flow and heat transfer of highly subcooled flow boiling in vertical upflow, Int. J. Heat Mass Transf. 136 (2019) 1199–1216.
[40] R. Raj, C. Kunkelmann, P. Stephan, J. Plawsky, J. Kim, Contact line behavior for a highly wetting fluid under superheated conditions, Int. J. Heat Mass Transf. 55 (2012) 2664–2675.
[41] R. Mei, J.F. Klausner, Shear lift force on spherical bubbles, Int. J. Heat Fluid Flow 15 (1994) 62–65.
[42] S.L. Sharma, T. Hibiki, M. Ishii, C.S. Brooks, J.P. Schlegel, Y. Liu, J.R. Buchanan, Turbulence-induced bubble collision force modeling and validation in adiabatic two-phase flow using CFD, Nucl. Eng. Des. 312 (2017) 399–409.
[43] X. Sun, Ph.D. thesis, Purdue University, 2001.
[44] M. Ishii, N. Zuber, Drag coefficient and relative velocity in bubbly, droplet or particulate flows, Am. Inst. Chem. Eng. J. 25 (1979) 843–855.
[45] S. Mohammed, M. Shah, a general correlation for heat transfer during subcooled boiling in pipes and annuli, Am. Soc. Heat., Refrig. Air-Condition. Engineers Trans. 83 (1977) 202–217.